journal___

Characterization of Ceramics by X-Ray and Neutron Small-Angle Scattering

Andrew J. Allen*,†

Ceramics Division, National Institute of Standards and Technology, Gaithersburg, Maryland 20899

This paper reviews some recent advances in small-angle X-ray and neutron scattering methods and their application to address complex issues in ceramic systems of technological importance. It is shown how small-angle scattering (SAS) can be applied to ceramic systems in order to extract statistically representative microstructure information (e.g., void volume fraction size distributions, internal surface areas, pore morphologies) that complements the information obtained from diffraction methods, X-ray microtomography, or electron microscopy. It is demonstrated how SAS studies provide insights, not obtainable by other means, on the processing–microstructure–property relationships that frequently govern technological performance.

I. Introduction

IN ongoing efforts to develop new nanotechnologies, advanced ceramics are being incorporated into increasingly complex and diverse heterogeneous systems.[1–4] The behavior and performance of these systems frequently depends on their multicomponent internal microstructure. Thus, optimizing and fine-tuning the microstructure can be the key to exploiting the material properties competitively in emerging technological applications. In fact microstructure (or nanostructure) is frequently the underlying link between the processing or service-life variables, and the overall observed material properties or device performance. New methods must continually be sought to meet the ever more demanding needs to characterize and quantify microstructures, and relate these to the processing variables so that the latter may be optimized. In this context, the analysis of the small-angle scattering (SAS) exhibited by a X-ray or neutron beam passing through a sample (small-angle X-ray scattering (SAXS) or small-angle neutron scattering (SANS)) has become one of the established means for determining and quantifying the statistically representative microstructures of heterogeneous materials.[5–36] The quantitative parameters obtained complement the visual information gained from scanning and transmission electron microscopy (SEM and TEM), computed X-ray microtomography (XMT), the phase composition information obtained from X-ray and neutron diffraction (XRD and ND), or information from other methods ranging from nuclear magnetic resonance (NMR) to light scattering.[37–52]

SAS has played a role in materials research since the development of laboratory SAXS methods by Guinier and others in the 1950s.[53–56] SANS became available at neutron research reactors from the mid-1960s onwards, and more especially with the development of large-scale cold-neutron facilities from the early 1970s,[57] and again in the 1990s.[58] More recently, SANS instruments have also been developed to utilize relatively short-wavelength neutrons and exploit the time structure at the major pulsed neutron facilities.[59] With the advent of modern synchrotron radiation X-ray facilities, SAXS methods have undergone a renaissance,[60–64] and both SAXS and SANS now exist in several specialized forms, designed to take advantage of the X-ray or neutron beam characteristics at major X-ray and neutron facilities for specific kinds of application.[65–69] These instruments are generally made available to a wide cross-section of industrial, government, and academic researchers through peer-reviewed research proposal systems. Furthermore, a number of innovative standalone SAXS instruments, using $CuK\alpha$ X-ray sources, are now available in the laboratory for industrial materials research.[70]

In general, conventional SAXS and SANS probe the microstructure scale regime from around 1 nm to approximately 100 nm.[71–73] Characteristics of SAXS are that it uses small beams (submillimeter down to a micrometer), it is best suited to thin (100 μm or less) sample materials having low to intermediate atomic number density for low absorption but intermediate to high atomic number density for scattering contrast, and it can benefit from the extreme brightness of a X-ray synchrotron source which provides excellent photon counting statistics.[68] Characteristics of SANS are that it utilizes larger beams (typically 5–20 mm dimension), it can penetrate samples up to a few millimeters thick, and it can exploit the strong fluctuations through the periodic table in the neutron scattering contrast, including isotope effects, to measure microstructures not easily detected by SAXS.[57,58,74] Sensitivity both to magnetic phenomena and to the presence of hydrogen, together with the ability to use polarized neutrons with aligned magnetic moments, are other important aspects of SANS.[75,76]

Feature

There is now a considerable body of literature based on SAS studies of metals and alloys, polymers, colloids and suspensions, as well as biological systems.[54,56,72,73] Characterization of ceramic materials by SAS has developed more slowly with two-thirds of the archival journal literature less than 10 years old. The reasons for this are twofold. Firstly, the microstructures of many conventional ceramic materials of technological interest tend to be coarse in length-scale and sufficiently concentrated in nature that significant multiple scattering issues need to be addressed in SAS analysis.[77–82] Secondly, the incorporation of ceramics into systems having a structure at the nanoscale level has accelerated in the last decade, driven by efforts in nanotechnology, and nanostructured ceramics suffer less from multiple scattering than do conventional ceramics.[83–85]

To address the challenges associated with multiple scattering and the presence of coarse microstructures, the technique of multiple SANS (MSANS) has been developed to recover the structural information from SANS studies using long-wavelength (cold) neutrons.[65,66,78–80,86–89] Furthermore, ultrasmall-angle X-ray and neutron scattering (USAXS and USANS) methods, which employ the so-called Bonse–Hart geometry, can extend the maximum feature size into the micrometer scale regime for USAXS, and to >10 μm for USANS.[40,90] Other advances include the development of high-energy SAXS (HE-SAXS) at the 3rd generation X-ray synchrotrons, which allows SAXS microstructure and diffraction phase composition data to be obtained for thicker X-ray samples during the same experiment.[91,92] At more modest X-ray energies, "anomalous" SAXS (ASAXS) studies vary the energy close to an X-ray absorption edge in order to vary the scattering contrast of one microstructure component against another.[93] Such studies can be analogous to "contrast variation" measurements in SANS where the neutron scattering isotope effect is exploited to somewhat similar effect.[94] Finally, the use of a grazing incidence (GI-) or "near-surface" (NS-) SAXS or SANS geometry enables the microstructure to be measured within a thin film or coating *in situ* on the substrate. This kind of SAS measurement has a similar geometry to, but is quite distinct from, X-ray or neutron reflectivity studies of thin films and surface features.[67,95]

Taking advantage of these developments, SAS studies of ceramic systems now represent a growing field with major research activities in areas that include: structural and electronic ceramics and glasses;[26–29,43–50,94,96–116] perovskites, high T_C superconductors, solid oxide fuel cells (SOFCs) and H storage materials;[4,75,117–125] sintering, cavitation and damage effects;[5–11,40–42,86,126–142] nanostructured and fractal solids and suspensions;[30,31,51,52,76,82–85,90,143–166] interfaces, membranes, thin films and coatings;[3,12–16,21–25,34,167–178] alloy/polymer/ceramic composites;[1,2,17–20,179–187] fine ceramics and archeology;[36] and cement and concrete science.[188–215] Unifying aspects that run through much of this work are the need to quantify the microstructure over many length scales, and to connect representative phenomena observed at micrometer and nanometer length-scales.

In this paper, some of the recent advances in SAXS and SANS methods are reviewed, together with examples that demonstrate their relevance to current ceramic applications of technological interest. Through these examples it is sought to show how SAS studies can provide insights, not obtainable by other means, on the processing–microstructure–property relationships that govern materials performance.
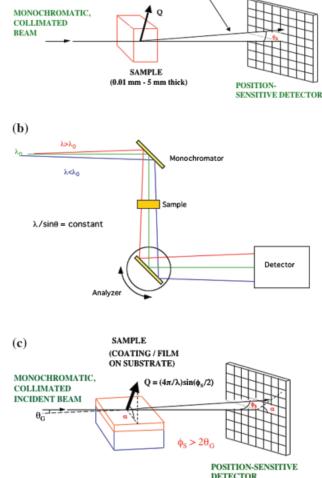
II. Essential Theoretical Background

Figure 1 shows schematically the three basic measurement geometries used in SAS studies. In each case a well-collimated incident beam impinges on the sample position and a small component of this incident beam is scattered out of the forward direction by a small angle. Except in the case of SANS at a pulsed neutron source, the incident beam is monochromatic. At a pulsed neutron source, the different wavelengths (energies)

Fig. 1. Basic schematics of the principal small-angle scattering (SAS) measurement configurations. (a) Transmission geometry configuration for small-angle neutron scattering (SANS) or small-angle X-ray scattering (SAXS) with a 2D detector. (b) Bonse–Hart configuration for ultra SANS or ultra SAXS. Note that in a practical instrument multiple reflections must occur both before and after the sample. (c) Reflection geometry configuration for SANS or SAXS. Note that for a finite grazing-incidence angle, θ_G, the minimum scattering angle, ϕ_S, for valid SAXS data is determined by the specular reflection: $2\theta_G$; also note that SAS in the reflection plane gives, primarily, structural information normal to the substrate while SAS measured at other azimuthal angles, α, provides structural information out of this normal direction. (Fig. 1b, Courtesy of John Barker, NCNR, NIST, Gaithersburg, MD.)

present are distinguishable by their different times of flight, and each time-resolved wavelength component can be considered as monochromatic. In any measurement, the SAS raw data are corrected for sample attenuation, detector sensitivity, parasitic and background scattering, effects because of the sample geometry, and are also usually calibrated against the incident beam intensity. The resulting scattered intensity profile, as a function of the scattering angle, is then a form of Fourier transform of the microstructure (or nanostructure) within the sample. To quantify the scattering in terms of the material properties rather than the details of a particular experiment, the normalized scattered intensity is given in terms of the differential SAS cross-section as a function of the scattering vector.[71–73] Definitions of these and other terms follow.

The scattering vector, **Q**, bisects the incident and scattered beams, and has magnitude, Q, given by: $Q = (4\pi/\lambda)\sin(\phi_S/2)$ where λ is the X-ray or neutron wavelength and ϕ_S is the angle of scatter. For a transmission geometry and small scattering angles, **Q** is nearly perpendicular to the incident beam direction and lies approximately in the plane of the sample. The scattered

intensity is expressed as the differential SAS cross-section per unit sample volume, $d\Sigma/d\Omega$, which is defined as the probability per unit X-ray or neutron flux, and per unit sample volume, of scattering into unit solid angle about the scattered beam direction described by the magnitude and direction of $\mathbf{Q}$. The relationship between $d\Sigma/d\Omega$ and the material microstructure is described in detail elsewhere.[53–56,71–73] Just the main results are summarized here. For most practical purposes, the scattering associated with a given $\mathbf{Q}$ is given by:

$$\frac{d\Sigma}{d\Omega}(\mathbf{Q}) = v_S^{-1}\left|\int_{v_S}\rho(\mathbf{r})\exp(i\mathbf{Q}\cdot\mathbf{r})\,d^3\mathbf{r}\right|^2 \qquad (1)$$

where $\rho(\mathbf{r})$ denotes the spatial variation of the X-ray or neutron coherent scattering length density within the sampling volume, v_S, over which the integral is taken. The X-ray or neutron scattering length, b, of any given element (for X-rays, the coherent scattering form-factor at zero scattering angle) is a fundamental property of the interaction between each radiation and a single atom. For X-rays, $b = 0.28z$ where z is the atomic number and b is in units of 10^{-14} m. For neutrons, b is typically an order of magnitude smaller, but the strong isotope effect and wide variation of b through the periodic table requires that it be obtained from published data tables.[74]

For a microstructure comprising a particulate morphology that is randomly oriented (isotropic), or at least circularly symmetric about the incident beam direction:[54]

$$\frac{d\Sigma}{d\Omega} = n|\Delta\rho|^2 V_P^2 F^2(Q)P(Q) \qquad (2)$$

where n is the number density of the particles, each with volume, V_P, while $|\Delta\rho|^2$ is the scattering contrast, $|F^2(Q)|$ is the scattering form-factor term for the individual particles, and $P(Q)$ is the effective structure factor for the arrangement of particles within the sampling volume. The scattering contrast, $|\Delta\rho|^2$, is the squared difference in the X-ray or neutron scattering length density, ρ, between that of the scattering particles and that of the surrounding medium. While Eq. (2) appears to describe only particulate microstructures, form- and structure-factor functions have been derived to enable the SAS from a wide range of heterogeneous morphologies to be described and quantified. Note that the SAS analysis is independent of the sign of $\Delta\rho$ in moving from a scattering feature to the surrounding medium. Thus, Eq. (2) applies equally well to voids within a solid medium as it does to solid particulates in air or suspended in an aqueous medium. While full details are available elsewhere,[53–56,71–73] some results are summarized below for special cases in order to clarify the information content that can be extracted from SAS measurements.

For a dilute concentration of scattering features having radius of gyration, R_G ($R_G^2 = 3R_S^2/5$ for a sphere of radius, R_S), the Guinier approximation applies for the scattering regime where QR_G is less than or order of unity:

$$\frac{d\Sigma}{d\Omega}_{QR_G\leq1} = \Phi_V|\Delta\rho|^2 V_P \exp\left(-\frac{Q^2 R_G^2}{3}\right) \qquad (3)$$

where the total volume fraction, $\Phi_V = nV_P$. Equation (3) indicates that, while scattering occurs at all Q, the most significant variation with Q in $d\Sigma/d\Omega$ occurs for objects of size R_G when Q is of order $1/R_G$. In the Guinier regime, R_G can be obtained from a straight-line fit to a plot of $\ln(d\Sigma/d\Omega)$ versus Q^2 for which the slope is $-R_G^2/3$.

In order to characterize the complex microstructures encountered in ceramic systems, one practical approach[22] is to assume the microstructure as comprised of scattering spheroids (voids or solid grains) with a given aspect ratio, β, orthogonal radii, R_O, R_O, βR_O, volume fraction size distribution, $\Phi(R_O)$, and orientation distribution, $W(\alpha,\omega)$. Here, $W(\alpha,\omega)$ is a probability distribution for the βR_O spheroid axis orientation, in terms of a polar angle, α, and an azimuthal angle, ω, measured, respectively, from the incident beam direction and one convenient direction within the sample plane. With respect to Eq. (3), $\Phi(R_O)$ integrates to Φ_V over the size distribution, $W(\alpha,\omega)$ integrates to unity over all solid angles, and $R_G^2 = (2+\beta^2)R_O^2/5$ for a spheroid. For such a system $d\Sigma/d\Omega$ is given by:[216]

$$\frac{d\Sigma}{d\Omega} = 6\pi^2|\Delta\rho|^2\beta\int_0^\infty dR_O\int_0^{2\pi}\sin\alpha\,d\omega$$
$$\times\int_0^{\pi/2}d\alpha\left\{\Phi(R_O)W(\alpha,\omega)R_O^3\left|\frac{J_{3/2}(u)}{u^{3/2}}\right|^2\right\} \qquad (4)$$

where $u = QR_O K(\beta,X)$, $K(\beta,X) = \{1+(\beta^2-1)X^2\}^{1/2}$, $J_{3/2}(u)$ denotes a Bessel function of order 3/2 such that $\{[J_{3/2}(u)]^2/u^3\} = \{(2/\pi)[\sin u-u\cos u]^2/u^6\}$, and $X = \cos\eta$ where η is the angle between the βR_O spheroid axis and the direction of $\mathbf{Q}$. By suitable choice of aspect ratio (shape), size, and orientation distributions, a wide range of microstructures can be modeled using Eq. (4). Different scattering form-factor terms, $|F^2(Q)|$ have been derived for other shapes of the individual scattering features, such as rods, disks, networks, shells, etc.[71,217–219] For many situations algorithms also exist to determine the size distributions present.[220–223] For a non-random orientation distribution of scattering features, analysis of the anisotropic SAS exhibited can be carried out, for example, by using a non-random form of $W(\alpha,\omega)$ in Eq. (4).

The scattering structure factor term, $P(Q)$, in Eq. (2) describes spatial correlations that may exist between (neighboring) scattering features. It is beyond the scope of this article to give a detailed description of all the possible forms of $P(Q)$ that may be encountered. However, two special cases serve to illustrate the information obtainable from $P(Q)$. When a population of uniform particles or voids is evenly distributed at a high volume concentration (>10%), $P(Q)$ modulates the overall $d\Sigma/d\Omega$ variation as a function of Q, to give a small-angle diffraction interference peak with a maximum at $2\pi/D$ where D is the mean separation distance between neighboring particles or voids, as measured in the direction of $\mathbf{Q}$.[54]

Another special case occurs for microstructures that exhibit fractal scaling or scale invariance over part of the scale range. Two kinds of fractal microstructure show distinct SAS hallmarks: volume- or mass-fractals, and surface-fractals, or self-affine surfaces. For mass-fractals, the mass within a radius, R, scales as R^{D_V} where $1<D_V<3$ such that $D_V = 1$ represents some form of chain and $D_V = 3$ represents a monolithic space-filling solid. The scattering varies as Q^{-D_V}. For surface fractals, the measured surface area within a radius R on the surface plane scales as R^{D_S} where $2<D_S<3$ such that $D_S = 2$ indicates a smooth surface and $D_S = 3$ represents a surface sufficiently convoluted that it fills a 3D volume. For a truly convoluted surface morphology, fractal in three dimensions, the scattering may show attributes of a mass fractal. However, in the more usual case of a self-affine surface where the scale invariance is confined to the approximate plane of the surface, the scattering varies as $Q^{-(6-D_S)}$. Thus, mass fractals are characterized by non-integral scattering power laws between Q^{-1} and Q^{-3} (but usually steeper than Q^{-2}), while surface fractals (or self-affine surfaces) are characterized by non-integral scattering power laws between Q^{-3} and Q^{-4}. Scattering formalisms have been derived to extract volume fraction, size, or total surface area information from mass- and surface-fractal scattering data, and to combine fractal structures with other microstructure components.[224–228]

In the limit of high Q, such that QL is large for any chord-length, L, within one scattering feature, the terminal slope in the scattered intensity becomes proportional to the internal surface area of the scattering features per unit sampling volume, S_V, and the Porod scattering law is obeyed:[55,71]

$$\frac{d\Sigma}{d\Omega}_{Q\to\infty} = \frac{2\pi|\Delta\rho|^2 S_V}{Q^4} + \text{BGD} \qquad (5)$$
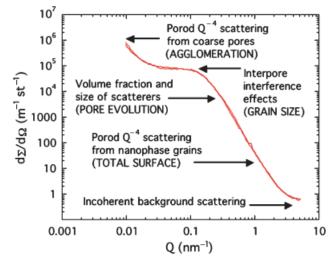
Fig. 2. Typical, absolute-calibrated, $d\Sigma/d\Omega$ small-angle neutron scattering data versus Q for a partially sintered nanoparticulate zirconia system[30] showing some of the scattering hallmarks described in the text, together with the generic information obtainable through use of an interpretative model. The model fit achieved here is also shown.

where BGD is the flat background parasitic scattering. In the case of an anisotropic orientation distribution, the Porod scattering must be orientationally averaged over all solid angles in order to recover the above relationship. However, once orientationally averaged, Eq. (5) holds at high Q, regardless of details of the scattering morphology, and both S_V and BGD can be obtained as the intercept and slope, respectively, from a straight line fit to a plot of $Q^4 d\Sigma/d\Omega$ versus Q^4.

Finally, it is sometimes useful in SAS studies to exploit the so-called "scattering invariant" in order to determine the absolute volume fraction of a scattering phase or, by combining it with Eq. (5), to obtain the surface area per unit volume if the scattering contrast is not well-known. The scattering invariant is given by:[71]

$$2\pi^2 \Phi_V (1 - \Phi_V) |\Delta\rho|^2 = \int_0^\infty Q^2 \frac{d\Sigma}{d\Omega}(Q) dQ \qquad (6)$$

(Note the $2\pi^2$ factor, not 2π as in Eq. (5).) Caution is required in applying the scattering invariant to experimental data because of the need to extrapolate the integral in Eq. (6) beyond the measured Q range both at low Q and at high Q (where the flat background must be removed and the remaining SAS data are frequently noisy). Nevertheless, a combination of Eqs. (5) and (6) can play a critical role if the microstructure and contrast are unknown.

In summary, SAS methods provide quantitative information on the statistically representative microstructure: void morphologies in solid materials, or particulate morphologies in powders, suspensions, or flames. Primary and secondary size distributions, particle–particle or void–void correlations, absolute volume fractions and surface areas, as well as anisotropic orientation distributions can all be quantified. Normally, SAS studies complement other measurements, with SAS quantifying the qualitative picture gained by other techniques such as electron microscopy. However, SAS can occasionally provide more deterministic primary information. For mono-dispersed systems in shape or size, the different forms of $|F^2(Q)|$ for spheres, cubes, tetrahedra, rods, discs, filled shells, etc., are well-known and distinctly different.[71,217–219] Certain secondary morphologies also exhibit distinctive hallmarks: extended rod-like or tubular structures, e.g., well-dispersed (unbundled) nanotubes should show a Q^{-1} scattering dependence; extended sheet-like structures should show a Q^{-2} dependence; and the hallmarks of fractal microstructures or the appearance of interference effects as a result of ordering have already been discussed. Sometimes,

the presence or absence of these characteristics in SAS data allow the overall statistically representative character of a microstructural ensemble to be assessed.

Figure 2 presents typical SAS data for a partially densified nanostructured ceramic oxide to illustrate selected general features discussed above for a particulate system. It remains to describe how different kinds of SAS experiment are carried out, and to demonstrate how SAS methods have been applied in research that supports advanced ceramic technology development.

III. Review of Experimental Methods

(1) SAS Using a 2D Position-Sensitive Detector

Figure 3 shows a modern SANS instrument based at a steady-state (research reactor) neutron source.[58] A liquid H moderator installed within the reactor vessel provides a source of "cold" neutrons having long de Broglie wavelengths ranging from 0.5 to 2.0 nm. Neutrons are brought from the cold source to the SANS instrument via Pt/Rh waveguides. The speed of the rotating helical monochromator at the front end of the instrument is set to pass neutrons of the desired wavelength with a (typical) 10%–15% band pass. A variable arrangement of collimators and further waveguides between the monochromator and the sample position provide the desired incident beam angular resolution. The neutron beam size at the sample position can range in diameter from under 1 mm to over 20 mm, depending on the size of sample. In the usual transmission SANS geometry, the sample is parallel sided and of thickness from around 0.5 mm up to a few millimeters, depending on the sample material. Together with the neutron wavelength, the distance from the sample to the large 2D position-sensitive detector (usually a multiwire mesh, filled with ^{3}He gas) determines the Q range for a given instrument set-up. Together with the detector pixel resolution (typically 5 mm), the sample-to-detector distance also determines the scattered beam angular resolution. The overall Q-resolution is optimized when the incident and scattered beam angular resolutions are approximately equal, and this means that the sample-to-detector distance and the distance from the exit aperture of the last incident waveguide to the sample are roughly comparable.

Usually two to three settings of the instrument geometry are required to obtain $d\Sigma/d\Omega$ over the full Q range attainable (0.05 nm^{-1} to several nm^{-1}) to characterize a complex microstructure. Over this Q range the SAS intensity may vary from above 10^{-2} of the incident beam intensity down to below 10^{-7}. The 2D detector must have a dynamic linear response over this range, and it must usually be protected from exposure to the un-attenuated incident beam intensity by a beam-stop positioned in front of the detector to absorb the incident beam. However, the beam-stop is removed and the incident beam attenuated by an absorber in order to determine the fraction of the incident beam intensity transmitted by the sample, and also to locate the position on the 2D detector of the un-scattered beam. The SAS data are corrected to allow for effects because of the sample and detector geometries, variations in the detector pixel sensitivity, sample absorption and other attenuation, and for background parasitic scattering effects. To obtain the sample scattering cross-section, $d\Sigma/d\Omega$, as a function of Q, the SAS data are circularly or sector-averaged. Then the data are calibrated against data from a scattering standard measured under similar conditions or, increasingly common nowadays, the SAS data may be calibrated directly against the incident beam intensity using the definition above for $d\Sigma/d\Omega$ with a known standard attenuator protecting the 2D detector. Once $d\Sigma/d\Omega$ data are obtained as a function of Q, one or more of the expressions above may be employed to extract the microstructure information.

At an accelerator-based pulsed neutron facility,[59,229] the rotating helical monochromator is replaced by one or more neutron choppers, and time-of-flight methods are used to separate out the different wavelength components. Advantages of making SANS measurements at a pulsed neutron source are that the
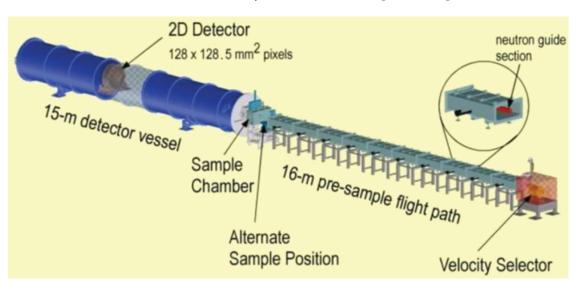
Fig. 3. Layout of the NIST/ExxonMobil[‡]/University of Minnesota NG7 small-angle neutron scattering instrument at the NIST Center for Neutron Research, National Institute of Standards and Technology, Gaithersburg, Maryland.[58] (Courtesy of NCNR, NIST, Gaithersburg, MD.)

higher neutron energies generally used penetrate further through thick samples, and the fully accessible Q range can be studied in a single instrument configuration. Disadvantages are generally higher background scattering and a comparatively low flux of cold neutrons that provide the microstructure information at the large-scale end of the accessible size range. However, these issues should be addressed from 2007 with SANS facilities being constructed at what will become the world's most powerful Spallation Neutron Source at Oak Ridge National Laboratory, Oak Ridge, Tennessee.[230]

While conventional SAXS instruments have measurement geometries broadly similar to that for SANS, important differences lie in the use of single-crystal diffraction optics to provide a highly monochromatic and collimated incident X-ray beam.[70] Other differences are that the incident X-ray flux is many times greater than even the best neutron flux, the X-ray wavelength used is of order 0.1 nm or shorter, the sample thickness (100–200 μm) is typically 10 times thinner than for SANS, and the incident beam size can have submillimeter dimensions. Nowadays, the 2D position-sensitive detector is usually a CCD with a pixel resolution of a few micrometers. These points tend to make SAXS instruments significantly more compact than their SANS counterparts. Lab-based SAXS instruments, using a CuKα rotating anode X-ray source, tend to be permanently set up and are frequently dedicated to support a specialized service function.[70] At a synchrotron, SAXS has traditionally been part of a shared beam line application, periodically assembled and disassembled to make way for other experiments. This situation is rapidly changing and most SAS facilities at synchrotron sources will be permanently set up in the future. Apart from the obvious flux advantage of synchrotron sources, the X-ray energy, E, can generally be tuned to any energy from below 5 keV to well above 20 keV. This corresponds to a wavelength range from 0.25 nm down to 0.06 nm (where $E = hc/\lambda$ with h = Planck's constant and c = the speed of light). While, at a synchrotron, λ can be chosen so as to provide a desired Q range, sample absorption effects can be large both at long λ (less penetrating low E) and at short λ (if a X-ray absorption edge energy is exceeded). Thus, sometimes limits restrict the choice of λ.

As with SANS the Q range and resolution depend on details of the instrument set-up. While broadly similar to SANS, the Q range is more limited at high Q by parasitic scattering and signal-to-noise issues. The 2D CCD SAXS detector must be protected from the incident beam intensity or it can suffer serious damage. This and the thin sample requirement (typically <0.2 mm

for ceramics) can make absolute intensity calibration more difficult for SAXS than for SANS. The need for universally accepted and versatile scattering standards for SAXS, particularly for the increasing number of laboratory SAXS systems based on CuKα sources, remains an issue that needs to be more fully addressed by the SAS community.[231]

(2) SAS Using Crystal Diffraction Optics

A SAS instrument configuration, radically different from the conventional instrumentation described above and with the resolution decoupled from the beam size, was first proposed by Bonse and Hart.[232] It exploits the small angular divergence of single-crystal Bragg diffraction to extend the SAS Q-range down to much lower Q, hence providing characterization of significantly larger scale features. However, it is only in recent years that the Bonse–Hart configuration for ultra SAS of both X-rays and neutrons (USAXS and USANS) has become fully competitive with conventional SAS in count rate and in versatility.[93,233]

Figure 4 presents a schematic of the Bonse–Hart USAXS instrument built by NIST at the UNICAT sector 33-ID at the Advanced Photon Source, Argonne National Laboratory.[64,68,69] At this 3rd generation synchrotron undulator beamline, the intense X-ray beam from the undulator is monochromatized by crystal optics, and harmonic wavelength contamination is removed through the use of harmonic rejection mirrors. In the experimental hutch, the sample is mounted between two multiple-reflection crystal monoliths. Within each monolith the crystal gap is set to accommodate either four or six Bragg diffractions. Without a sample present, the Darwin rocking-curve profile of the transmitted beam, as measured by the photodiode detector while the second analyzer monolith is rotated out of the Bragg condition, has a width of only a few arc-seconds. It exhibits strongly suppressed rocking-curve tails $-Q^{-8}$ or Q^{-12}. With a sample present, part of the SAXS component continues to satisfy the Bragg condition as the analyzer monolith (after the sample) is rotated, and the photodiode detector registers a scattered intensity that is significantly higher than given by the Darwin profile tail. The USAXS intensity can be recovered by subtracting out the rocking curve data with no sample present, after allowing for beam attenuation in the sample. The linear dynamic response range of the photodiode extends over more than 10 decades in X-ray intensity. This is sufficient to measure both the full incident beam intensity when the analyzer monolith satisfies the Bragg condition for the incident beam ($Q = 0$), and the sample SAS, transmitted through the analyzer monolith as it is rotated away from the Bragg condition. The analyzer rotation angle is also the USAXS scattering
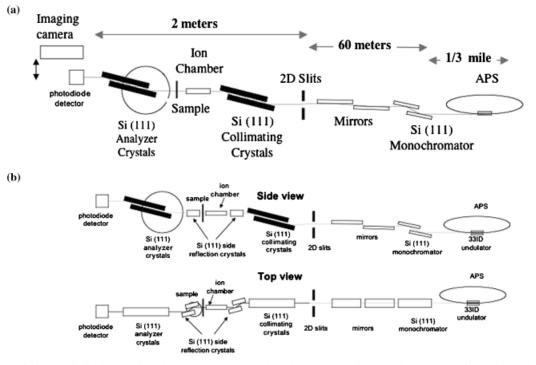
Fig. 4. Schematic of the NIST-built ultra small-angle X-ray scattering (USAXS) instrument at the UNICAT sector 33 of the Advanced Photon Source, Argonne National Laboratory, Argonne, Illinois.[68] (a) Side view of the regular slit-smeared USAXS configuration. The analyzer crystal monolith is rotated out of the Bragg condition for the incident beam by the scattering angle, ϕ_S, in order to record the SAXS data (measured with the photodiode) as a function of Q (downward and approximately in the sample plane). The imaging camera is used to survey samples into position or for USAXS imaging. (b) Side and top views of the anisotropic USAXS configuration incorporating side reflection crystals to remove the slit-smearing effect perpendicular to the USAXS Q scanning direction. The imaging camera is omitted for clarity. (Courtesy of Pete Jemian, University of Illinois at Urbana-Champagne, IL, and Jan Ilavsky, APS XOR, ANL, Argonne, IL, modified by the author.)

angle, ϕ_S from which Q is defined. The analyzer monolith and detector are moved downwards as ϕ_S is increased and the direction of **Q** is approximately downwards in the plane of the sample.

In the standard instrument configuration (Fig. 4(a)), the data are intrinsically slit-smeared because the collimation only matches the rocking curve width in the diffraction plane. In the transverse direction the collimation is determined by the angle subtended by the detector aperture at the sample position. However, for an isotropic microstructure, USAXS data are readily desmeared by well-established methods.[234] The attainable Q-range is from 0.001 nm^{-1} up to more that 1 nm^{-1}, with the maximum Q usually determined by signal-to-noise issues, rather than the geometric instrument configuration. The large linear dynamic response enables an absolute intensity calibration of the data to give $d\Sigma/d\Omega$ as a function of Q without the need for a scattering standard. For anisotropic microstructures, an effective pinhole collimation can be achieved by the addition of two transverse side reflection stages, as shown in Fig. 4b.[69] This has the effect of providing Darwin width rocking curve collimation in both the vertical and horizontal planes. The Q scanning direction remains downwards as it is only in the vertical plane that the rocking curve tails are suppressed by the multiple Bragg reflections within each of the collimating and analyzer crystal monoliths. The anisotropic USAXS configuration results in a decreased counting intensity, and consequently the maximum obtainable Q is reduced to typically around 0.3 nm^{-1}. However, the anisotropic sample can be rotated in the sample plane and successive USAXS scans made with arbitrarily fine azimuthal angular resolution.

In principle, the significantly narrower crystal rocking curve Darwin widths encountered in neutron diffraction, compared with X-ray diffraction, permit the USANS Q-range to extend down almost to 0.0001 nm^{-1}, virtually a magnitude below the minimum Q for USAXS.[235] Unfortunately, two major obstacles have hindered the practical development of USANS until the last 10 years. The very much lower neutron flux available at even the best neutron sources, compared with the high X-ray

brilliance of the synchrotron X-ray sources, has severely limited USANS count rates, and precluded a practical sample throughput. More seriously, the low neutron absorption in the diffracting crystals results in a high scattering background associated with crystal back-wall reflections that manifest themselves as intolerably high apparent rocking curve tails. Recently, the latter problem has been eradicated by adjusting the crystal geometry so as to shield against parasitic back-wall reflections.[236] At the NIST NCNR, the low flux issue has also been addressed by using a bent graphite monochromator that provides the required USANS angular and λ-resolution in the diffracting plane, but allows a large angular permittance in the orthogonal plane. Taking advantage of these innovations,[233] the NIST USANS instrument at NCNR, provides a practical throughput of four to six samples per day and a Q range from 0.0001 to 0.03 nm^{-1}, which overlaps with conventional SANS. Given these recent innovations, both USAXS and USANS will likely play an increasingly significant role in future SAS applications and development.

(3) Specialized SAS Measurement Configurations
Various specialized SAS measurement configurations have been developed to address particular classes of problem that are relevant to advanced ceramics research:

(A) Contrast Variation SANS: The isotope effect in neutron scattering can be used to vary the SANS scattering contrast to identify scattering components within a heterogeneous or hydrogeneous system.[74] As an example, the neutron coherent scattering-length density, ρ, of H_2O is -0.568×10^{14} m^{-2} (m/m^3) while that of D_2O is $+6.58 \times 10^{14}$ m^{-2}. Thus, in a system containing water, the ratio between H_2O and D_2O can be varied until the SANS intensity vanishes (or is minimized). The known H_2O/D_2O ratio then permits calculation of ρ for the liquid phase, which, at the contrast match point, is the same as for the scattering phase. The situation is more complex if the scattering phase also includes an exchanging H/D sub-component as

in cement systems, but SANS contrast variation still provides a powerful tool for interrogating the system.[212]

(B) ASAXS: While there is no isotope effect to be exploited in SAXS, ASAXS studies can differentiate between different scattering phases if the X-ray energy is varied close to that of a "X-ray absorption edge" for an element contained within one of the scattering phases.[5,93,126,223] The absorption edge is characterized by a sharp resonant increase in X-ray absorption with increasing X-ray energy as K- or L-shell atomic electrons are excited. The increase in absorption can be associated with anomalous variations in both the real and imaginary parts of the X-ray scattering form-factor. By following these changes as a function of X-ray energy just below the absorption edge, it is possible to distinguish scattering components by the different degrees of ASAXS response according to their atomic composition.

(C) High-Energy Small- and Wide-Angle X-Ray Scattering (WAXS): Below the X-ray absorption edge, attenuation of the X-ray beam because of absorption decreases with increasing X-ray energy. Above the absorption edge, attenuation because of absorption is much increased. Indeed the X-ray penetration depth does not recover until a much higher X-ray energy is used. For example, in the case of yttria-stabilized zirconia (YSZ), the Y and Zr absorption edges are at just below 17 keV and just below 18 keV, respectively. Above these energies, the X-ray penetration does not match that found at 16.9 keV until the X-ray energy is above 35 keV.[237] Thus, most SAXS and USAXS studies of YSZ systems are best carried out with an energy below 17 keV. However, the relatively recent development of X-ray undulators and high energy focusing optics at 3rd generation X-ray synchrotrons, has opened up opportunities to work with primary X-ray energies as high as 40 keV, and with harmonics up to 80 keV, or even 120 keV.[91,92] The use of such high X-ray energies has two major advantages. The X-ray absorption is greatly reduced, permitting greater sample thicknesses in the millimeter range (i.e. comparable with neutron sample thicknesses) to be usable for many materials. Secondly the basic instrument geometry for HE-SAXS can be maintained for comparison diffraction measurements of composition and crystalline phase in so-called high-energy WAXS (HE-WAXS). At such high X-ray energies, a complete diffraction pattern can be registered on a 2D CCD detector using a measurement geometry that is virtually unchanged from HE-SAXS. When combined with a small beam size (down to micrometer dimensions in one direction) HE-SAXS and HE-WAXS studies can be made to correlate the microstructure and phase variations with position through a layered or gradient system such as a SOFC section.[238]

(D) MSANS: As pointed out in the Introduction, many conventional ceramic materials contain coarse, concentrated void morphologies. Reference to Eq. (3) shows how this can lead to significant multiple scattering as the single-scatter SAS cross-section is proportional both to the volume fraction of scatterers, Φ_V, and to the mean individual scatterer volume, V_P. Methods have been developed to correct for multiple scattering effects when these are small.[239] However, these methods are not appropriate when there is copious multiple scattering broadening of the incident beam such as occurs when each X-ray or neutron is scattered on average many times as it passes through the sample. Multiple scattering effects can be estimated from the total scattering probability on integrating $d\Sigma/d\Omega$ over all solid angle and multiplying by the sample thickness, τ_S. Large τ_S, Φ_V, V_P, or a long X-ray or neutron λ can produce copious multiple scattering beam broadening, the last of these because long λ implies (through the definition of Q) that $d\Sigma/d\Omega$ is high over a large solid angle. Using the long λ available at a neutron cold source, the copious MSANS broadening can be exploited to derive scattering size information not normally obtainable by single scattering because it would occur at Q values too small to be in the instrument measurement range. The MSANS broadening actually brings this information into the accessible measurement range. At NIST, an MSANS formalism has been developed to extract void size information from the variation in MSANS broadening with λ.[65,66,78,79,86,89] The method, which

also takes into account the effects of refraction from large scattering features, has been successfully applied to elucidate sintering phenomena in various technologically important ceramic systems,[11,82] including thermal barrier coatings (TBCs) for advanced gas turbines.[22,174]

(E) Reflection Geometry SAS: Finally, the increasingly important need for microstructure characterization within thin films and coatings, *in situ* on the substrate, should be recognized. The internal structure of such films and coatings, as a function of both the processing conditions and the service environment, has a critical effect on their properties and function.[25] Various reflection geometry SAS measurement configurations have evolved, including GI-SAXS[67] and NS-SANS.[95] Unlike techniques such as reflectivity which characterize a surface by exploring the regime where the GI angle, θ_G is both greater and less than the critical grazing angle for total reflection at an interface, θ_C, GI-SAXS and NS-SANS use a fixed $\theta_G > \theta_C$ and explore the internal film or coating microstructure by measuring the SAS from the incident beam component transmitted into the coating. While the different wavelengths and scattering lengths applicable for SAXS and SANS make θ_C, typically $<0.5°$, broadly comparable for GI-SAXS and NS-SANS (as hence are the measurement geometries), the different absorption coefficients result in different penetration depths: tens of nanometers for GI-SAXS, tens of micrometers for NS-SANS. Thus, NS-SANS is suitable for studies of (e.g.) relatively thick TBCs, while GI-SAXS is better matched to studies of dielectric layers and other electronic coatings. In either case, such measurements must overcome various challenges. For example, as neutrons or X-rays pass into the sample at grazing incidence, they deviate because of significant refraction effects at the interface. These SAS methods complement other grazing geometry techniques such as GI diffraction and reflectivity.[12,39,240] Indeed, the development of instrumentation, which would provide such measurements simultaneously, or at least sequentially, for a single sample configuration is currently underway at some of the X-ray synchrotron facilities. This type of SAXS application is growing in importance,[241] not only to characterize thin films and dielectric coatings, but also other planar architectures relevant to functional ceramic nanotechnology, such as quantum dot layers or aligned C nanotubes deposited on a substrate.

IV. Examples of Application

To date SAS methods have contributed to four main overlapping areas of research that support the materials development of functional ceramics, together with an increasing contribution to advanced cement and concrete research. In this section, the role played by SAS methods in each area is summarized. Some selected examples are described in more detail.

(1) Structural/Electronic Ceramics and Glasses, Perovskite Applications

SAS methods have characterized and quantified many of the defect morphologies that control the desired properties of structural and electronic ceramics and glasses.[4,26–29,43–50,75,94,96–125] These include perovskite materials of current interest for SOFC applications and for high-T_C superconductors. In order to distinguish between the frequently present multiple component microstructures SANS studies can exploit the neutron isotope effect for one or more of the components, or exploit the neutron magnetic interaction with any atoms within a component that possess a finite magnetic moment. In the latter case, polarized SANS studies can amplify the effects observed when a magnetic field is applied. For SAXS studies, the ASAXS at X-ray energies close to a specific element's X-ray absorption edge can be exploited to distinguish between components. Using such tools, SAS methods have successfully interrogated the thermodynamics and kinetics of the component microstructures in ceramic and glass materials to address both fabrication and performance issues.

One advanced application of SAS has been the use of polarized neutrons in SANS investigations of high-T_C superconductors. Using a polarized neutron beam produced by magnetic alignment of the neutron spins (magnetic moments), Gordeyev et al.[75] reported the first observation of small-angle polarized neutron scattering (SAPNS) from magnetic flux inhomogeneities in high-T_C Y–Ba–Cu–O and La–Sr–Cu–O ceramics. The difference between the scattering cross sections for neutrons initially polarized along or opposite to the applied field was measured at $T < T_C$ over a range of field strengths below the critical field, H_C. An opposite effect was observed for the remanent field trapped in the grains after the applied field was switched off. The studies were used to elucidate nuclear-magnetic interferences within the superconductors, together with the associated magnetic-nuclear neutron scattering-length density fluctuations—information pertaining to superconductor performance uniquely obtained by SANS.

(2) Sintering, Cavitation, and Damage Effects

SAS methods have addressed a range of void characterization issues in ceramic materials development,[5–11,40–42,86,126–142] such as elucidating aspects of the pore evolution during sintering, or quantifying the void defect and cavitation morphology that develops as a result of creep or other damage effects. The evolution of the void size distribution during the sintering and densification of nanostructured ceramics and gels has been comprehensively studied by both SANS and SAXS. For the measurement of sintering, microcracking, cavitation, or creep damage on the micrometer scale, USAXS and MSANS methods have proven useful because of their ability to obtain information about features larger than 1 μm. Furthermore, anomalous USAXS studies have differentiated between multiple populations of creep-induced void cavities and precipitates of similar size.

One of the more cited studies was carried out by Luecke et al.,[5] which combined anomalous USAXS studies of creep in hot isostatically pressed (HIPed) silicon nitride, with corresponding TEM and mechanical property measurements. These authors were able to quantify the size distribution of the creep cavities, demonstrate that cavity addition, rather than cavity growth, dominates the cavitation process, and relate the results to the available creep models for granular materials. The USAXS studies, specifically, established that cavitation at the multigrain junctions, rather than that generally on grain boundaries, plays a critical role in allowing the silicate to flow from cavities to surrounding silicate pockets, thus accommodating the dilatation of the microstructure and deformation of the material. This same study quantified the underlying differences between tensile and compressive creep deformation. Although 10 years old, the work remains highly relevant to the continued consideration of silicon nitride for advanced technology applications such as in land-based gas turbines.

(3) Interfaces, Membranes, Thin Films, Coatings, and Composites

The sensitivity of SAS methods to the scattering from internal surfaces and interfaces has resulted in their application to quantify microstructures with high interface densities such as found in nanocomposites or within precipitate morphologies.[1–3,12–25,34,167–187] This is of particular importance when the physical or chemical properties are determined by such interfaces. Membranes, films, and coatings also fall into this category and have been the subject of several SAS investigations using conventional SANS and SAXS, USAXS and MSANS methods.

By illustration, Fig. 5 shows results from an anisotropic MSANS study of the microstructure in a self-standing, plasma-sprayed, YSZ deposit typical of TBCs used in advanced gas turbines.[22] A combination of precision density measurements, anisotropic Porod scattering and MSANS analysis was used to distinguish the three principal anisotropically oriented void components that are the hallmarks of plasma-spray deposits:
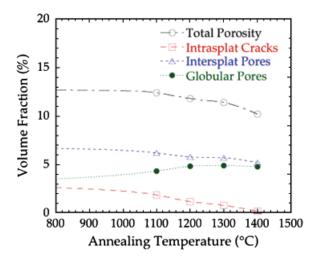

Fig. 5. Multiple small-angle neutron scattering-derived total and component void porosities versus 1 h annealing temperature for a plasma-sprayed yttria-stabilized zirconia thermal barrier coating.[22] Fractional experimental uncertainties are around 5% for each data point. The analysis also yielded the corresponding mean dimensions and surface areas for each component.

intersplat planar pores predominantly parallel to the substrate, intrasplat cracks predominantly perpendicular to the substrate, and globular pores distributed throughout the microstructure. The mean opening dimension, volume fraction, surface area, and orientation distribution were determined for each component. Using numerical-based microstructure models these data were correlated with TBC mechanical and thermal properties such as elastic modulus and thermal conductivity. Figure 5 shows the total and component volume fractions as a function of annealing for 1 h at each at the temperatures indicated. A relative loss of intrasplat crack porosity and an increase in the globular porosity are indicated, while the intersplat lamellar pores mainly persist. The preferential annealing or sintering out of the intrasplat cracks at temperatures as low as 800°C was not previously detected prior to the SANS and MSANS studies. However, these changes (together with those determined for the void dimensions and surface areas) are symptomatic of those that will occur within a TBC under operating conditions. They are not quantitatively measurable for the component void morphologies by any other means.

For electron-beam physical vapor-deposited (EB-PVD) TBCs (used to coat the hottest moving parts in advanced gas turbines), the fine void morphologies and gradient microstructures make them most amenable to study by the anisotropic USAXS method (see Fig. 4b), because of the small synchrotron X-ray beam size. A thin (150 μm) section of sample and substrate, cut perpendicular to the substrate, can be studied in a transmission geometry. The EB-PVD system is characterized by a columnar structure, strongly aligned perpendicular to the substrate. The void microstructure consists of intercolumnar voids, intracolumnar cracks and "feather" pores, and a dispersed nanoporosity that may be partially associated with the feather morphology. Some of the component void systems exhibit strongly anisotropic orientation distributions that are distinct from each other. These are revealed by setting the USAXS analyzer at a given $\mathbf{Q}$, then rotating the sample within the sample plane to measure the anisotropy in the SAXS intensity versus orientation. Figure 6 shows a resulting anisotropic intensity plot with contributions from the component morphologies indicated.[242] Also shown are some selected USAXS images. These were obtained by using the X-ray CCD camera to view the sample with the analyzer monolith set at the given $\mathbf{Q}$, thus imaging the sample with the USAXS intensity, itself. Different parts of the microstructure light up depending on their orientation and position in the coating (and also the Q value for different feature sizes), thus providing a powerful method for surveying the sample

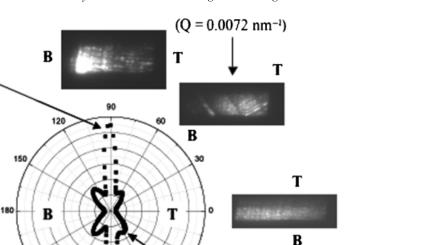**Fig. 6.** Anisotropic ultra small-angle X-ray scattering (USAXS) plot of scattered intensity versus sample azimuthal angle for an electron-beam physical vapor-deposited microstructure, showing the scattering from some of the principal void component features.[242] Also shown are USAXS images of the microstructure at selected sample azimuthal angles, obtained using the imaging camera with the analyzer stage rotated to $Q = 0.006$ nm^{-1}. The sample orientation is shown in the images by T and B to indicate the top and bottom of the coating. In the main plot T and B indicate the zero reference orientation for the azimuthal rotation of **Q**. The USAXS images indicate that the most pronounced intercolumnar void structure occurs near the bottom of the coating. Because of the uniform distribution of feather voids within them, the columns are illuminated throughout the coating at the preferred sample orientation for scattering from the feather voids. Also apparent is the 3-layer character of the coating caused by some densification at the top of each component layer during thermal cycling at 1150°C. None of these points are discernible in regular radiographic images at $Q = 0$.

into position at a selected orientation for USAXS studies. This is necessary because the USAXS data for such complex anisotropic microstructures must be measured for many orientations both of **Q** and of the sample itself (i.e., the USAXS data must be over-determined), and the data must be simultaneously fit using a multi-component microstructure model. Meanwhile, the USAXS imaging method has been fully developed elsewhere as a new form of materials X-ray imaging technique, providing yet another new SAS application.[243]

The use of small (few micrometers) X-ray beams at the 3rd generation synchrotron X-ray sources provides new opportunities for the study of gradient microstructures such as are found in SOFC systems.[238] However, the need to accommodate a thin coating or film on its substrate has spurred significant innovative instrument developments in recent years. GI-SAXS and NS-SANS measurements, both made in reflection geometry, have met with some success in addressing this need. Furthermore, these methods can be readily combined with X-ray or neutron reflectivity measurements of the surface structure, and GI diffraction studies of the phase composition. Sometimes, diffuse scattering measurements can also be made of the large-scale microstructure fluctuations parallel to the substrate within the film or coating, especially if measured around and relative to a small-angle diffraction peak at a finite **Q** where the data are more readily analyzable than at zero absolute Q.[12]

(4) Nanostructured/Fractal Materials and Suspensions

The ability of SAS methods to quantify structures over an extended scale regime from nanometers to micrometers has made them particularly suitable as a diagnostic tool in new mate-

rials development for nanotechnology.[30,31,51,52,76,82–85,90,143–166] Whereas electron microscopy provides detailed local information for a nanostructured or nanoparticulate morphology, SAXS and SANS provides complementary, quantitative, microstructure information that is statistically representative over macroscopic sampling volumes. Thus, nucleation, growth, coarsening, aggregation and sintering phenomena have all been followed, quantitatively, as a function of time, temperature, or other external condition. SAS methods have also been applied in the study of zeolites and catalysts, solution-mediated colloids, gels and suspensions, and for nanoparticle ensembles that include soot or silica particles in flames.[244] Furthermore, the statistically representative nature of the size, volume-fraction, and surface-area information obtained has been related directly to the scale-invariant properties of disordered fractal microstructures such as found in geological materials or cements.

SAS methods are finding application in current efforts to control and optimize the aqueous mediated manipulation of nanoparticle assemblies and dispersions for incorporation into functional ceramic devices. These include studies of single- and multi-walled C nanotubes for both electronic and bio-medical applications,[245] and other nanoparticle drug delivery systems.[246] Figure 7 presents a schematic of a USAXS flow cell developed by the author with collaborators. Flowing fluid suspensions can be studied in real time under known conditions of controlled temperature, flow rate, pH, and/or added solvent concentration. Figure 8 presents preliminary USAXS data obtained through use of the flow cell to follow controlled nanoparticle nucleation and growth in a precipitating ceria system. The data reveal both nucleation and growth of the particles, together with indications of a shell-like ordered structure that may be developing on the particle surfaces. Using such a flow cell and SAS methods to
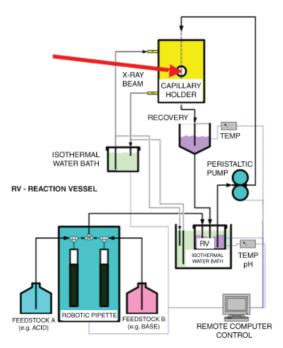
Fig. 7. Schematic of NIST ultra small-angle X-ray scattering (USAXS) fluid flow cell layout for real-time studies of solution-mediated nanoparticle systems and suspensions. Driven by a peristaltic pump, the sample flows through a 1.5 mm diameter capillary at the X-ray beam position. Temperature, flow rate, pH, and/or solvent concentration can all be controlled remotely and continuously monitored. (Courtesy of Pete Jemian, University of Illinois at Urbana-Champagne, IL.)

quantify the real-time nucleation, growth, agglomeration and interaction, self-assembly, and dissolution of ceramic nanoparticles, under known controlled conditions, is proposed to support a range of potential applications including solution mediated nanoparticle drug delivery development.

(5) Advanced Cement and Concrete Research

The nanoscale porosity and fractal nature of the calcium–silicate–hydrate (CSH) gel that is the main product of cement hydration has been the subject for a significant body of SAS studies in cement and concrete research.[188–215] The amorphous nature of CSH gel, together with its intimate relationship to the water of hydration, has enabled SAS methods, (especially SANS) to characterize its microstructure and evolution during cement hydration. This area of application can combine many aspects discussed above: fractal structures over an extended
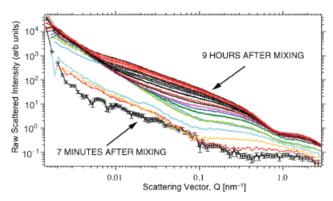

Fig. 8. Preliminary (slit-smeared) ultra small-angle X-ray scattering (USAXS) data showing the effects of nucleation and growth of a precipitating nanoparticle ceria suspension, under controlled dispersant conditions. Changes in the USAXS curves are caused by the nucleation and growth processes, together with the presence of some shell-like ordering on the particle surfaces and elsewhere.

scale range, contrast variation SANS (where both the solid and aqueous phases undergo H/D isotope exchange), real-time and long-term microstructure evolution with hydration, drying or chemical leaching, etc. A detailed description of these cement studies would extend beyond the focus of this article, but the cited reference list might provide useful information to the interested reader.

V. Concluding Remarks and Future Prospects

This article has sought to highlight recent advances in SAS methods and their ongoing contributions to research supporting advanced technological ceramic development. An increasing diversity in SAS method development is evident, and the need for optimizing microstructure design to enhance the performance of various functional ceramic-based systems provides a driving force for many of these efforts.

For SAXS, the availability of small intense X-ray beams at 3rd generation synchrotron sources makes possible the ability to interrogate gradient microstructures and internal interfaces within multi-component systems such as SOFCs as has not been possible hitherto. The high X-ray brilliance also allows microstructure changes to be followed in real-time to increasingly small subsecond time-resolution. Similarly, the use of reflection geometry SAXS now provides the opportunity to characterize the microstructures of thin (nanometer) films *in situ* on the substrate, much more comprehensively than previously possible, so opening up new possibilities in materials research for electronic and optoelectronic applications. The increasing availability of high-energy X-rays in HE-SAXS increases the X-ray depth penetration to that usually associated with SANS, and makes possible simultaneous microstructure and phase structure determinations. [In this context it is fortunate that parasitic double Bragg scattering, which can affect SAXS studies of materials with a large coherent crystallite size (e.g., metals and alloys, or single crystals),[247] is not usually significant for ceramic materials with their relatively fine crystallite size and broader mosaic spread.]

By comparison, SANS research remains more heavily weighted towards metals and alloys (especially magnetic materials) and polymer systems. However, the high penetrability of neutrons greatly enhances their usefulness for the characterization of composite systems, many of which include a critical ceramic component. Both the neutron isotope effect and the neutron magnetic moment interaction provide research tools for specific applications. The USANS method currently provides access to the lowest Q values (down to 10^{-4} nm^{-1}) and hence can measure the largest scattering features (>10 μm). Furthermore, much information can be gained by combining SANS with other inelastic neutron-based methods that interrogate kinetic issues not tractable by other means. While neutron fluxes are unlikely to approach the photon fluxes of the most powerful X-ray sources, new facilities such as the Spallation Neutron Source, under construction at Oak Ridge National Laboratory, Oak Ridge, TN, will provide SANS time resolutions to significantly better than 1 min.

Finally, the increasing number of industrial SAXS facilities, now available from several commercial suppliers, will provide a much closer connection, over the next few years, between SAS methods and functional materials development. As one of an array of newly available industrial characterization tools for advanced materials development, the need to establish universally accepted SAS intensity and wavelength standards, traceable to a primary calibration method, is likely to become ever more urgent. It should also be emphasized that SAS is but one generic method of materials characterization among many others being developed or enhanced to meet the challenges of the new nano- and biotechnologies. It will be in devising new ways of using these various advanced diagnostic measurement techniques together that the greatest new material advances will most likely occur.

Acknowledgments

References

[1]A. C. Finnefrock, R. Ulrich, G. E. S. Toombes, S. M. Gruner, and U. Wiesner, "The Plumbers Nightmare: A New Morphology in Block Copolymer–Ceramic Nanocomposites and Mesoporous Aluminosilicates," *J. Am. Chem. Soc.*, **125**, 13084–93 (2003).

[2]J. E. Mark, "Ceramic-Modified Elastomers," *Curr. Opin. Solid State Mater. Sci.*, **4**, 565–70 (1999).

[3]J. F. Janik, W. C. Ackerman, R. T. Paine, D. W. Hua, A. Maskara, and D. M. Smith, "Boron-Nitride as a Selective Gas Adsorbent," *Langmuir*, **10**, 514–8 (1994).

[4]R. Petricevic, M. Glora, and J. Fricke, "Planar Fibre Reinforced Carbon Aerogels for Application in PEM Fuel Cells," *Carbon*, **39**, 857–67 (2001).

[5]W. E. Luecke, S. M. Wiederhorn, B. J. Hockey, R. F. Krause, and G. G. Long, "Cavitation Contributes Substantially to Tensile Creep in Silicon-Nitride," *J. Am. Ceram. Soc.*, **78**, 2085–96 (1995).

[6]K. S. Chan and R. A. Page, "Creep Damage Development in Structural Ceramics," *J. Am. Ceram. Soc.*, **76**, 803–26 (1993).

[7]C. R. Blanchard and K. S. Chan, "Evidence of Grain-Boundary-Sliding-Induced Cavitation in Ceramics Under Compression," *J. Am. Ceram. Soc.*, **76**, 1651–60 (1993).

[8]J. E. Mark, "Some Recent Theory, Experiments, and Simulations on Rubberlike Elasticity," *J. Phys. Chem. B*, **107**, 903–13 (2003).

[9]M. H. Zimmerman, D. M. Baskin, K. T. Faber, E. R. Fuller, A. J. Allen, and D. T. Keane, "Fracture of a Textured Anisotropic Ceramic," *Acta Mater.*, **49**, 3231–42 (2001).

[10]H. Vesteghem, A. Lecomte, and A. Dauger, "Film Formation and Sintering of Colloidal Monoclinic Zirconia," *J. Non-Cryst. Solids*, **147**, 503–7 (1992).

[11]G. G. Long, S. Krueger, R. A. Gerhardt, and R. A. Page, "Small-Angle Neutron-Scattering Characterization of Processing Microstructure Relationships in the Sintering of Crystalline and Glassy Ceramics," *J. Mater. Res.*, **6**, 2706–15 (1991).

[12]O. Robach, G. Renaud, and A. Barbier, "Structure and Morphology of the Ag/MgO (001) Interface During In Situ Growth at Room Temperature," *Phys. Rev. B*, **60**, 5858–71 (1999).

[13]R. S. A. Delange, J. H. A. Hekkink, K. Keizer, and A. J. Burggraaf, "Polymeric-Silica-Based Sols for Membrane Modification Applications—Sol–Gel Synthesis and Characterization with SAXS," *J. Non-Cryst. Solids*, **191**, 1–16 (1995).

[14]T. J. Su, J. R. Lu, Z. F. Cui, R. K. Thomas, and R. K. Heenan, "Application of Small Angle Neutron Scattering to the In Situ Study of Protein Fouling on Ceramic Membranes," *Langmuir*, **14**, 5517–10 (1998).

[15]A. C. Mitropoulos, K. Beltsios, T. A. Steriotis, F. K. Katsaros, P. Makri, and N. K. Kanellopoulos, "The Combination of Equilibrium and Dynamic Methods for the Detailed Structural Characterisation of Ceramic Membranes," *J. Eur. Ceram. Soc.*, **18**, 1545–58 (1998).

[16]T. J. Su, J. R. Lu, Z. F. Cui, B. J. Bellhouse, R. K. Thomas, and R. K. Heenan, "Identification of the Location of Protein Fouling on Ceramic Membranes Under Dynamic Filtration Conditions," *J. Membr. Sci.*, **163**, 265–75 (1999).

[17]D. W. McCarthy, J. E. Mark, S. J. Clarson, and D. W. Schaefer, "Synthesis, Structure, and Properties of Hybrid Organic–Inorganic Composites Based on Polysiloxanes. II. Comparisons Between Poly(Methylphenylsiloxane) and Poly(Dimethylsiloxane), and Between Titania and Silica," *J. Polym. Sci. B*, **36**, 1191–200 (1998).

[18]F. W. Embs, E. L. Thomas, C. C. J. Wung, and P. N. Prasad, "Structure and Morphology of Sol–Gel Prepared Polymer–Ceramic Composite Thin-Films," *Polymer*, **34**, 4607–12 (1993).

[19]D. Kurtenbach, H. P. Martin, E. Muller, G. Roewer, and A. Hoell, "Crystallization of Polymer Derived Silicon Carbide Materials," *J. Eur. Ceram. Soc.*, **18**, 1885–91 (1998).

[20]J. M. Breiner, J. E. Mark, and G. Beaucage, "Dependence of Silica Particle Sizes on Network Chain Lengths, Silica Contents, and Catalyst Concentrations in In-Situ-Reinforced Polysiloxane Elastomers," *J. Polym. Sci. B*, **37**, 1421–7 (1999).

[21]J. Ilavsky, A. J. Allen, G. G. Long, S. Krueger, C. C. Berndt, and H. Herman, "Influence of Spray Angle on the Pore and Crack Microstructure of Plasma-Sprayed Deposits," *J. Am. Ceram. Soc.*, **80**, 733–42 (1997).

[22]A. J. Allen, J. Ilavsky, G. G. Long, J. S. Wallace, C. C. Berndt, and H. Herman, "Microstructural Characterization of Yttria-Stabilized Zirconia Plasma-Sprayed Deposits Using Multiple Small-Angle Neutron Scattering," *Acta Mater.*, **49**, 1661–75 (2001).

[23]A. Kulkarni, Z. Wang, T. Nakamura, S. Sampath, A. Goland, H. Herman, A. J. Allen, J. Ilavsky, G. G. Long, J. Frahm, and R. W. Steinbrech, "Comprehensive Microstructural Characterization and Predictive Property Modeling of Plasma-Sprayed Zirconia Coatings," *Acta Mater.*, **51**, 2457–75 (2003).

[24]J. Ilavsky, G. G. Long, A. J. Allen, L. Leblanc, M. Prystay, and C. Moreau, "Anisotropic Microstructure of Plasma-Sprayed Deposits," *J. Thermal Spray Technol.*, **8**, 414–20 (1999).

[25]A. J. Allen, G. G. Long, H. Boukari, J. Ilavsky, A. Kulkarni, S. Sampath, H. Herman, and A. N. Goland, "Microstructural Characterization Studies to Relate the Properties of Thermal-Spray Coatings to Feedstock and Spray Conditions," *Surf. Coat. Technol.*, **146**, 544–52 (2001).

[26]W. H. Gu, K. T. Faber, and R. W. Steinbrech, "Microcracking and R-Curve Behavior in SiC–TiB$_2$ Composites," *Acta Metal. Mater.*, **40**, 3121–8 (1992).

[27]S. Schempp, J. Durr, P. Lamparter, J. Bill, and F. Aldinger, "Study of the Atomic Structure and Phase Separation in Amorphous Si–C–N Ceramics by X-Ray and Neutron Diffraction," *Z. Nat. A*, **53**, 127–33 (1998).

[28]A. F. Wright, A. N. Fitch, J. B. Hayter, and B. E. F. Fender, "Nucleation and Crystallization of Cordierite TiO$_2$ Glass Ceramic. 1. Small-Angle Neutron-Scattering Measurements and Simulations," *Phys. Chem. Glasses*, **26**, 113–8 (1985).

[29]J. Bill, J. Schuhmacher, K. Muller, S. Schempp, J. Seitz, J. Durr, H. P. Lamparter, J. Golczewski, J. Q. Peng, H. J. Seifert, and F. Aldinger, "Investigations into the Structural Evolution of Amorphous Si–C–N Ceramics from Precursors," *Z. Metall.*, **91**, 335–51 (2000).

[30]A. J. Allen, S. Krueger, G. Skandan, G. G. Long, H. Hahn, H. M. Kerch, J. C. Parker, and M. N. Ali, "Microstructural Evolution During the Sintering of Nanostructured Ceramic Oxides," *J. Am. Ceram. Soc.*, **79**, 1201–12 (1996).

[31]I. Betz, A. Sturm, J. F. Loffler, W. Wagner, A. Wiedenmann, and H. Hahn, "Microstructural Development During Final-Stage Sintering of Nanostructured Zirconia Based Ceramics," *Mater. Sci. Eng. A*, **281**, 68–74 (2000).

[32]P. Fratzl, "Small-Angle Scattering in Materials Science—A Short Review of Applications in Alloys, Ceramics and Composite Materials," *J. Appl. Crystallogr.*, **36**, 397–404 (2003).

[33]P. Staron, D. Bellmann, R. Kampmann, M. Klatt, and R. Wagner, "Characterization of Microstructures with Sizes from the Sub-nm to the μm-Range by Extended Small-Angle Neutron Scattering," *Physica B*, **241**, 98–100 (1997).

[34]T. T. Borek, W. Ackerman, D. W. Hua, R. T. Paine, and D. M. Smith, "Highly Microporous Boron-Nitride for Gas-Adsorption," *Langmuir*, **7**, 2844–6 (1991).

[35]S. Mazumder, D. Sen, and A. K. Patra, "Characterization of Porous Materials by Small-Angle Scattering," *Pramana-J. Phys.*, **63**, 165–73 (2004).

[36]P. Fermo, F. Cariati, C. Cipriani, M. Canetti, G. Padeletti, B. Brunetti, and A. Sgamellotti, "The Use of Small Angle X-Ray Scattering (SAXS) for the Characterisation of Lustre Surfaces in Renaissance Majolica," *Appl. Surf. Sci.*, **185**, 309–16 (2002).

[37]K. W. Harbich, M. P. Hentschel, and J. Schors, "X-Ray Refraction Characterization of Non-Metallic Materials," *NDT and E Int.*, **34**, 297–302 (2001).

[38]M. P. Hentschel, A. Lange, B. R. Muller, J. Schors, and K. W. Harbich, "X-Ray Refraction Computer-Tomography," *Materialprufung*, **42**, 217–21 (2000).

[39]B. Pardo, F. Bridou, and M. Maaza, "X-Ray Reflectometry and Small-Angle Scattering," *J. Phys. IV*, **6** [C4] 351–66 (1996).

[40]V. Ryukhtin, J. Saroun, S. Harjo, Y. Motohashi, M. Baron, and R. Loidl, "Comparative Study of Porosity in 3Y-TZP Superplastic Ceramics by Ultra-Small-Angle Neutron Scattering and Scanning Electron Microscopy Image Analysis," *J. Appl. Crystallogr.*, **36**, 478–83 (2003).

[41]W. Wagner, R. S. Averback, H. Hahn, W. Petry, and A. Wiedenmann, "Sintering Characteristics of Nanocrystalline TiO$_2$—A Study Combining Small-Angle Neutron-Scattering and Nitrogen Absorption-BET," *J. Mater. Res.*, **6**, 2193–8 (1991).

[42]R. Neumann, "Scanning Probe Microscopy of Ion-Irradiated Materials," *Nucl. Instrum. Methods Phys. Res. B*, **151**, 42–55 (1999).

[43]T. I. Chuvaeva, O. S. Dymshits, V. I. Petrov, M. Y. Tsenter, A. V. Shashkin, A. A. Zhilin, and V. V. Golubkov, "Low-Frequency Raman Scattering of Magnesium Aluminosilicate Glasses and Glass–Ceramics," *J. Non-Cryst. Solids*, **282**, 306–16 (2001).

[44]N. V. Golubko, M. I. Yanovskaya, I. P. Romm, and A. N. Ozerin, "Hydrolysis of Titanium Alkoxides: Thermochemical, Electron Microscopy, SAXS Studies," *J. Sol-Gel Sci. Technol.*, **20**, 245–62 (2001).

[45]A. L. Korzhenevskii, "An Anomalous Increase of the Small-Angle Light-Scattering in Ferroelectric Ceramics Near the Phase-Boundary," *Ferroelectrics*, **100**, 39–42 (1989).

[46]U. Lembke, R. Bruckner, R. Kranold, and T. Hoche, "Phase Formation Kinetics in a Glass Ceramic Studied by Small-Angle Scattering of X-Rays and Neutrons and by Visible-Light Scattering," *J. Appl. Crystallogr.*, **30**, 1056–64 (1997).

[47]D. Sauter, M. Weinmann, F. Berger, P. Lamparter, K. Muller, and F. Aldinger, "X-Ray and Neutron Scattering and Solid State NMR Investigations on Precursor-Derived B–C–N Ceramics Using Isotopic Substitution," *Chem. Mater.*, **14**, 2859–70 (2002).

[48]J. Haug, P. Lamparter, M. Weinmann, and F. Aldinger, "Diffraction Study on the Atomic Structure and Phase Separation of Amorphous Ceramics in the Si–(B)–C–N System. 2. Si–B–C–N Ceramics," *Chem. Mater.*, **16**, 83–92 (2004).

[49]G. N. Greaves, W. Bras, M. Oversluizen, and S. M. Clarke, "A SAXS/WAXS XAFS Study of Crystallisation in Cordierite Glass," *Faraday Discuss.*, **122**, 299–314 (2003).

[50]O. S. Dymshits, A. A. Zhilin, V. I. Petrov, M. Y. Tsenter, T. I. Chuvaeva, A. V. Shashkin, V. V. Golubkov, U. Kang, and K. H. Lee, "A Raman Spectroscopic Study of Phase Transformations in Titanium-Containing Magnesium Aluminosilicate Glasses," *Glass Phys. Chem.*, **28**, 66–78 (2002).

[51]S. Botti, C. Cicognani, R. Coppola, A. Lapp, and M. Magnani, "Particle Size and Optical Performances of Photoluminescent Laser Synthesized Si Nanopowders," *Physica B*, **276**, 860–1 (2000).

[52]L. M. Colyer, G. N. Greaves, B. U. Komanschek, M. A. Roberts, A. J. Dent, K. K. Fox, and S. W. Carr, "Dynamic Observation of Crystallographic and Micro Structural Changes Associated with the Collapse and Recrystallisation of Cd Exchanged Zeolite-A," *Mater. Sci. Forum*, **228**, 363–8 (1996).

[53]A. Guinier, "Diffraction of X-Rays at Very Small Angles: Application to the Study of Ultramicroscopic Phenomena," *Ann. Phys. (Paris)*, **12**, 161–237 (1939).

[54]A. Guinier and G. Fournet, *Small-Angle Scattering of X-Rays*. John Wiley and Sons, New York, 1955.

[55]G. Porod, "X-Ray Low Angle Scattering of Dense Colloid Systems Part I," *Kolloid Z.*, **124**, 83–114 (1951) (Part II, 125, 108–22 (1952)).

[56]P. Debye, R. Anderson, and H. Brumberger, "Scattering by an Inhomogeneous Solid. II. The Correlation Function and its Application," *J. Appl. Phys.*, **28**, 679 (1957).

[57]K. Ibel, "The Neutron Small-Angle Camera D11 at High-Flux Reactor, Grenoble," *J. Appl. Crystallogr.*, **9**, 296–309 (1976).

[58]C. J. Glinka, J. Barker, B. Hammouda, S. Krueger, J. Moyer, and W. Orts, "The 30m SANS Instruments at NIST," *J. Appl. Crystallogr.*, **31**, 430–45 (1998).

[59]R. K. Heenan, J. Penfold, and S. M. King, "SANS at Pulsed Neutron Sources: Present and Future Prospects," *J. Appl. Crystallogr.*, **30**, 1140–7 (1997).

[60]G. G. Long, A. J. Allen, D. R. Black, H. E. Burdette, D. A. Fischer, R. D. Spal, and J. C. Woicik, "National Institute of Standards and Technology Synchrotron Radiation Facilities for Materials Science," *J. Res. Nat. Inst. Stand. Technol.*, **106**, 1141–54 (2001).

[61]H. Amenitsch, S. Bernstorff, M. Kriechbaum, D. Lombardo, H. Mio, G. Pabst, M. Rappolt, and P. Laggner, "The Small-Angle X-Ray Scattering Beamline at ELETTRA: A New Powerful Station for Fast Structural Investigations on Complex Fluids with Synchrotron Radiation," *Nuovo Cimenta Soc. Italia. Fisica D*, **20**, 2181–90 (1998).

[62]A. J. Allen, P. R. Jemian, D. R. Black, H. E. Burdette, R. D. Spal, S. Krueger, and G. G. Long, "Ultra Small Angle X-Ray Scattering to Bridge the Gap Between Visible Light Scattering and Standard SAXS Cameras," *Nucl. Instrum. Methods Phys. Res. A*, **347**, 487–90 (1994).

[63]C. Riekel, M. Burghammer, and M. Muller, "Microbeam Small-Angle Scattering Experiments and their Combination with Microdiffraction," *J. Appl. Crystallogr.*, **33**, 421–3 (2000).

[64]G. G. Long, A. J. Allen, J. Ilavsky, P. R. Jemian, and P. Zschack, "The Ultra-Small Angle X-Ray Scattering Instrument on UNICAT at the APS;" pp. 183–7 in *Synchrotron Radiation Instrumentation: Eleventh U.S. National Conference*, Edited by P. Pianetta, J. Arthur, and S. Brennan. AIP, Melville, NY, 2000.

[65]G. G. Long, S. Krueger, and A. J. Allen, "Multiple Small-Angle Neutron Scattering," *J. Neutron Res.*, **7**, 195–210 (1999).

[66]A. J. Allen, N. F. Berk, J. Ilavsky, and G. G. Long, "Multiple Small-Angle Neutron Scattering Studies of Anisotropic Materials," *Appl. Phys. A.*, **74** [Suppl.] S937–9 (2002).

[67]J. R. Levine, J. B. Cohen, Y. W. Chung, and P. Georgopoulos, "Grazing-Incidence Small-Angle X-Ray Scattering: New Tool for Studying Thin Film Growth," *J. Appl. Crystallogr.*, **22**, 528–32 (1989).

[68]J. Ilavsky, P. R. Jemian, A. J. Allen, and G. G. Long, "Versatile USAXS (Bonse–Hart) Facility for Advanced Materials Research," *AIP Conf. Proc.*, **705**, 510–3 (2004).

[69]J. Ilavsky, A. J. Allen, G. G. Long, and P. R. Jemian, "Effective Pinhole-Collimated Ultrasmall-Angle X-Ray Scattering Instrument for Measuring Anisotropic Microstructures," *Rev. Sci. Instrum.*, **73**, 1660–2 (2002).

[70]T. P. Rieker and P. F. Hubbard, "The University of New Mexico Sandia National Laboratories Small-Angle Scattering Laboratory," *Rev. Sci. Instrum.*, **69**, 3504–9 (1998).

[71]G. Porod, "General Theory;" pp. 17–51 in *Small-Angle X-ray Scattering*, Edited by O. Glatter and O. Kratky. Academic Press, London, 1982.

[72]G. Kostorz (ed.) *Treatise on Materials Science and Technology*, Vol. 15; pp. 227–87. Academic Press, New York, 1979.

[73]G. Kostorz, "Small-Angle Scattering Studies of Phase Separation and Defects in Inorganic Materials," *J. Appl. Crystallogr.*, **24**, 444–56 (1991).

[74]V. F. Sears, "Neutron Scattering Lengths and Cross Sections," *Neutron News*, **3** [3] 29–37 (1992).

[75]G. Gordeyev, A. Okorokov, V. Runov, M. Runova, B. Toperverg, A. Brulet, R. Kahn, R. Papoular, J. Rossat Mignod, H. Glattli, H. Eckerlebe, R. Kampmann, and R. Wagner, "Small-Angle Scattering of Polarized Neutrons in HTSC Ceramics," *Physica B*, **234**, 837–8 (1997).

[76]A. Wiedenmann, "Small-Angle Neutron Scattering Investigations of Magnetic Nanostructures Using Polarized Neutrons," *J. Appl. Crystallogr.*, **33**, 428–32 (2000).

[77]K. Hardman-Rhyne, N. F. Berk, and E. R. Fuller, "Microstructural Characterization of Ceramic Materials by Small-Angle Neutron-Scattering Techniques," *J. Res. Nat. Bur. Stand.*, **89**, 17–34 (1984).

[78]N. F. Berk and K. A. Hardman-Rhyne, "Characterization of Alumina Powder Using Multiple Small-Angle Neutron-Scattering. 1. Theory," *J. Appl. Crystallogr.*, **18**, 467–72 (1985).

[79]N. F. Berk and K. A. Hardman-Rhyne, "The Phase-Shift and Multiple-Scattering in Small-Angle Neutron-Scattering—Application to Beam Broadening from Ceramics," *Physica B & C*, **136**, 218–22 (1986).

[80]K. A. Hardman-Rhyne, K. G. Frase, and N. F. Berk, "Applications of Multiple Small-Angle Neutron-Scattering to Studies of Ceramic Processing," *Physica B & C*, **136**, 223–5 (1986).

[81]R. A. Page, "Applications of Small-Angle Scattering in Ceramic Research," *J. Appl. Crystallogr.*, **21**, 795–804 (1988).

[82]G. G. Long and S. Krueger, "Multiple Small-Angle Neutron-Scattering Characterization of the Densification of Ceramics—Application to Microporous Silica," *J. Appl. Crystallogr.*, **22**, 539–45 (1989).

[83]A. J. Allen, S. Krueger, G. G. Long, H. M. Kerch, H. Hahn, and G. Skandan, "Small-Angle Neutron Scattering Studies of Ceramic Nanophase Materials," *Nanostruct. Mater.*, **7**, 113–26 (1996).

[84]J. L. Shi, C. W. Lu, C. L. Kuo, Z. X. Lin, and T. S. Yen, "Determination of Crystallite Size of Superfine Zirconia Powders as a Function of Calcination Temperatures," *Ceram. Int.*, **18**, 155–9 (1992).

[85]U. Keiderling, A. Wiedenmann, V. Srdic, M. Winterer, and H. Hahn, "Nano-Sized Ceramics of Coated Alumina and Zirconia Analyzed with SANS," *J. Appl. Crystallogr.*, **33**, 483–7 (2000).

[86]A. J. Allen and N. F. Berk, "Analysis of Small-Angle Scattering Data Dominated by Multiple-Scattering for Systems Containing Eccentrically Shaped Particles or Pores," *J. Appl. Crystallogr.*, **27**, 878–91 (1994).

[87]Y. G. Abov, D. S. Denisov, N. O. Elyutin, S. K. Matveev, Y. I. Smirnov, A. O. Eidlin, F. S. Dzheparov, and D. V. L'vov, "Asymptotic Behavior of Neutron Small-Angle Multiple Scattering Spectra," *J. Exp. Theor. Phys.*, **87**, 1195–200 (1998).

[88]S. Mazumder, B. Jayaswal, and A. Sequeira, "The Inverse Problem in Multiple Small-Angle Scattering," *Physica B*, **241**, 1222–4 (1997).

[89]N. F. Berk and K. A. Hardman-Rhyne, "Analysis of SAS Data Dominated by Multiple-Scattering," *J. Appl. Crystallogr.*, **21**, 645–51 (1988).

[90]F. Triolo, A. Triolo, M. M. Agamalian, J. S. Lin, R. K. Heenan, G. Lucido, and R. Triolo, "Fractal Approach in Petrology: Combining Ultra Small Angle, Small Angle and Intermediate Angle Neutron Scattering," *J. Appl. Crystallogr.*, **33**, 863–6 (2000).

[91]X.-L. Wang, J. Almer, C. T. Liu, Y. D. Wang, J. K. Zhao, A. D. Stoica, D. R. Haeffner, and W. H. Wang, "*In situ* Synchrotron Study of Phase Transformation Behaviors in Bulk Metallic Glass by Simultaneous Diffraction and Small Angle Scattering," *Phys. Rev. Lett.*, **91**, 265501 (2003).

[92]S. D. Shastri, K. Fezzaa, A. Mashayekhi, W.-K. Lee, P. B. Fernandez, and P. L. Lee, "Cryogenically Cooled, Bent Double-Laue Monochromator for High-Energy Undulator X-Rays (50–200 keV)," *J. Synchrotron Rad.*, **9**, 317–22 (2002).

[93]G. G. Long, P. R. Jemian, J. R. Weertman, D. R. Black, H. E. Burdette, and R. D. Spal, "High-Resolution Small-Angle X-Ray-Scattering Camera for Anomalous Scattering," *J. Appl. Crystallogr.*, **24**, 30–7 (1991).

[94]J. Durr, S. Schempp, P. Lamparter, J. Bill, S. Steeb, and F. Aldinger, "X-Ray and Neutron Small Angle Scattering with Si–C–N Ceramics Using Isotopic Substitution," *Solid State Ionics*, **101**, 1041–7 (1997).

[95]W. A. Hamilton, P. D. Butler, J. B. Hayter, L. J. Magid, and P. J. Kreke, "'Over the Horizon' SANS: Measurements on Near-Surface Poiseuille Shear-Induced Ordering of Dilute Solutions of Threadlike Micelles," *Physica B*, **221**, 309–19 (1996).

[96]A. F. Wright, J. Talbot, and B. E. F. Fender, "Nucleation and Growth Studies by Small-Angle Neutron-Scattering and Results for a Glass Ceramic," *Nature*, **277**, 366–8 (1979).

[97]U. Lembke, A. Hoell, R. Kranold, R. Muller, W. Schuppel, G. Goerigk, R. Gilles, and A. Wiedenmann, "Formation of Magnetic Nanocrystals in a Glass Ceramic Studied by Small-Angle Scattering," *J. Appl. Phys.*, **85**, 2279–86 (1999).

[98]V. N. Sigaev, S. Y. Stefanovich, B. Champagnon, I. Gregora, P. Pernice, A. Aronne, R. LeParc, P. D. Sarkisov, and C. Dewhurst, "Amorphous Nanostructuring in Potassium Niobium Silicate Glasses by SANS and SHG: A New Mechanism for Second-Order Optical Non-Linearity of Glasses," *J. Non-Cryst. Solids*, **306**, 238–48 (2002).

[99]I. W. Donald, B. L. Metcalfe, and A. E. P. Morris, "Influence of Transition-Metal Oxide Additions on the Crystallization Kinetics, Microstructures and Thermal-Expansion Characteristics of a Lithium Zinc Silicate Glass," *J. Mater. Sci.*, **27**, 2979–91 (1992).

[100]A. Hoell, R. Kranold, U. Lembke, R. Bruckner, R. Muller, P. Gornert, and W. Schuppel, "Structural Investigation of Ferrimagnetic Particles Formed by Glass Crystallization," *Berich. Bunsen-Gesellsch.*, **100**, 1646–50 (1996).

[101]A. K. Bandyopadhyay, P. Labarbe, J. Zarzycki, and A. F. Wright, "Nucleation and Crystallization Studies of a Basalt Glass–Ceramic by Small-Angle Neutron-Scattering," *J. Mater. Sci.*, **18**, 709–16 (1983).

[102]L. S. Kamzina and N. N. Krainik, "Effect of Electric Field on the Percolation Phase Transition in Lead Scandotantalate Single Crystals," *Physics of the Solid State*, **42**, 142–5 (2000).

[103]U. Lembke, A. Hoell, R. Kranold, and R. Bruckner, "Small-Angle Scattering Investigation of Phase-Separation in Glasses Influenced by Admixtures of TiO_2, MoO_3 and WO_3," *J. Phys. IV*, **3** [C8] 329–32 (1993).

[104]P. A. Smith, H. M. Kerch, A. G. Haerle, and J. Keller, "Microstructural Characterization of Alumina and Silicon Carbide Slip-Cast Cakes," *J. Am. Ceram. Soc.*, **79**, 2515–26 (1996).

[105]V. N. Sigaev, "Structure of Oxide Glasses and Formation of Polar Glass–Ceramic Textures," *Glass Phys. Chem.*, **24**, 295–307 (1998).

[106]T. Kamiyama and K. Suzuki, "A SAXS Study of the Ceramization Process of Si–C Organic Precursor," *J. Non-Cryst. Solids*, **234**, 476–82 (1998).

[107]K. Suzuya, M. Furusaka, N. Watanabe, M. Osawa, K. Okamura, K. Shibata, T. Kamiyama, and K. Suzuki, "Mesoscopic Structure of SiC Fibers by Neutron and X-Ray Scattering," *J. Mater. Res.*, **11**, 1169–78 (1996).

[108]V. V. Golubkov, O. S. Dymshits, A. A. Zhilin, T. I. Chuvaeva, and A. V. Shashkin, "On the Phase Separation and Crystallization of Glasses in the MgO–Al_2O_3–SiO_2–TiO_2 System," *Glass Phys. Chem.*, **29**, 254–66 (2003).

[109]D. Enke, F. Friedel, F. Janowski, T. Hahn, W. Gille, R. Muller, and H. Kaden, "Ultrathin Porous Glass Membranes with Controlled Texture Properties," *Stud. Surf. Sci. Catal.*, **144**, 347–54 (2002).

[110]C. Penot, A. Fabre, P. Goursat, D. Bahloul, A. Lecomte, A. Dauger, and P. Lespade, "Thermolysis of Boron-Nitride Organo-Silicon Precursors," *An. de Chimie-Sci. Mater.*, **17**, 155–65 (1992).

[111]J. Haug, P. Lamparter, M. Weinmann, and F. Aldinger, "Diffraction Study on the Atomic Structure and Phase Separation of Amorphous Ceramics in the Si–(B)–C–N System. 1. Si–C–N Ceramics," *Chem. Mater.*, **16**, 72–82 (2004).

[112]K. Sinko and L. Poppl, "Transformation of Aluminosilicate Wet Gel to Solid States," *J. Solid State Chem.*, **165**, 111–8 (2002).

[113]K. W. Harbich and M. P. Hentschel, "Nondestructive Characterization of Monolithic Ceramics by X-Ray Refraction," *Key Eng. Mater.*, **206**, 673–6 (2002).

[114]K. Rainer, H. Armin, L. Ulrich, and M. Robert, "Characterization of Magnetic Nanocrystals in a Glass Ceramic by Small-Angle Neutron Scattering," *Glass Sci. Technol.—Glastech. Ber.*, **73**, 395–8 (2000).

[115]U. Lembke, R. Kranold, and R. Bruckner, "Characterization of Phase-Transformations in Glasses by Small-Angle Scattering of X-Rays and Neutrons," *Nucl. Instrum. Methods Phys. Res. B*, **97**, 194–7 (1995).

[116]D. Ravaine and A. F. Wright, "Concentration Fluctuations in a Rb_2O–SiO_2 Glass," *Phys. Chem. Glasses*, **24**, 31–4 (1983).

[117]D. Wang, J. D. Clewley, T. B. Flanagan, R. Balasubramaniam, and K. L. Shanahan, "The Interaction of Dissolved H with Internally Oxidized Pd–Rh Alloys," *Acta Mater.*, **50**, 259–75 (2002).

[118]A. I. Okorokov, V. V. Runov, A. D. Tretyakov, S. V. Maleev, and B. P. Toperverg, "Gas-Exchange with the Superconducting Ceramic $YBa_2Cu_3O_{7-delta}$ and its Fractal Properties Derived from Small-Angle Neutron-Scattering Data," *Zh. Eksp. I Teor. Fiz.ik*, **100**, 257–73 (1991).

[119]G. P. Kopitsa, V. V. Runov, and A. I. Okorokov, "Spin Correlations in $YBa_2(Cu_{(1-x)} Fe_x)_3O_{7+y}$ Ceramic," *Physics of the Solid State*, **40**, 19–22 (1998).

[120]G. P. Kopitsa, V. V. Runov, A. I. Okorokov, I. S. Lyubutin, and K. V. Frolov, "The Spin Correlations in $YBa_2(Cu_{1-x}Fe_x)_3O_{7-y}$ Ceramics at $T = 15$–500 K Investigated by the Small-Angle Scattering of Polarized Neutrons," *Physica B*, **297**, 245–9 (2001).

[121]G. P. Kopitsa, V. V. Runov, and A. I. Okorokov, "The Investigation of the Spin Correlations in $YBa_2(Cu_{(1-x)}Fe_x)_3O_{7-y}$ Ceramics by the Small-Angle Scattering of Polarized Neutrons," *Physica B*, **276**, 788–9 (2000).

[122]Y. G. Abov, Y. I. Smirnov, D. S. Denisov, N. O. Elyutin, S. K. Matveev, and A. O. Eidlin, "Using the Multiple Small-Angle Neutron-Scattering Technique to Study the Porosity Parameters of HTCS Ceramics," *Fizika Tverdogo Tela*, **34**, 1408–17 (1992).

[123]G. P. Kopitsa, V. V. Runov, A. I. Okorokov, I. S. Lyubutin, and K. V. Frolov, "Small-Angle Polarized Neutron Scattering in $YBa_2(Cu_{0.9}Fe_{0.1})_3O_{7-y}$ Ceramics at $T = 290$–550 K," *Appl. Phys. A*, **74**, S628–30 (2002).

[124]G. Kopitsa, V. Runov, and A. Okorokov, "The Observation of the Magnetic Correlations in $YBa_2(Cu_{1-x}Fe_x)_3O_{7+y}$ Ceramics by Small-Angle Polarized Neutron Scattering," *Physica B*, **234**, 839–40 (1997).

[125]H. W. Tian, J. F. Zang, T. Ding, W. T. Zheng, and X. Wang, "The Evidence of Phase Separation in Perovskite Manganites above T_c," *J. Wuhan Univ. Technol.—Mater. Sci. Ed.*, **19**, 62–3 (2004).

[126]F. Lofaj, S. M. Wiederhorn, G. G. Long, B. J. Hockey, P. R. Jemian, L. Browder, J. Andreason, and U. Taffner, "Non-Cavitation Tensile Creep in Lu-Doped Silicon Nitride," *J. Eur. Ceram. Soc.*, **22**, 2479–87 (2002).

[127]S. Harjo, N. Kojima, Y. Motohashi, J. Saroun, V. Ryukthin, P. Strunz, R. Loidl, and M. Baron, "Characterization of Cavities in Superplastically Deformed Tetragonal Zirconia Polycrystals by Means of Small Angle Neutron Scattering," *Mater. Trans.*, **43**, 2480–6 (2002).

[128]K. S. Chan and R. A. Page, "Transient Cavity Growth in Ceramics Under Compression," *J. Mater. Sci.*, **27**, 1651–8 (1992).

[129]M. Klatt, D. Bellmann, R. Kampmann, R. Wagner, C. Wolf, and H. Hubner, "SANS Investigation of Creep Pores in Liquid-Phase-Sintered Alumina," *Physica B*, **213**, 496–8 (1995).

[130]C. R. Blanchard, R. A. Page, and S. Spooner, "The Measurement of Compressive Creep Deformation and Damage Mechanisms in a Single-Phase Alumina—Part II—Correlation of Creep Cavitation and Grain Boundary Sliding," *J. Mater. Sci.*, **33**, 5049–58 (1998).

[131]U. S. Lindholm, "Experimental Mechanics—New Challenges in Micromechanics," *Mech. Mater.*, **10**, 31–42 (1990).

[132]M. Klatt, D. Bellmann, R. Kampmann, R. Wagner, C. Wolf, and H. Hubner, "Joint Use of Double Crystal Diffractometry, Beam Broadening and Conventional SANS for Analysis of Creep Pore Formation in Liquid-Phase Sintered Alumina," *Physica B*, **234**, 1019–21 (1997).

[133]S. Harjo, J. Saroun, Y. Motohashi, N. Kojima, V. Ryukthin, P. Strunz, M. Baron, and R. Loidl, "Flat Cavities Formed in TZP Caused by Superplastic Deformations at High Strain-Rates and their Effect on Elongation," *Mater. Trans.*, **45**, 824–32 (2004).

[134]R. A. Page and J. Lankford, "Characterization of Creep Cavitation in Sintered Alumina by Small-Angle Neutron Scattering," *J. Am. Ceram. Soc.*, **68**, C146–C148 (1983).

[135]D. Sen, A. K. Patra, S. Mazumder, and S. Ramanathan, "Pore Morphology in Sintered ZrO_2–8 mol% Y_2O_3 Ceramic: A Small-Angle Neutron Scattering Investigation," *J. Alloys Compounds*, **340**, 236–41 (2002).

[136]P. Harmat, L. Bartha, T. Grosz, and L. Rosta, "Sintered Materials Studied by Small-Angle Neutron Scattering," *Physica B*, **276**, 826–9 (2000).

[137]M. Klatt, D. Bellmann, R. Kampmann, R. Wagner, C. Wolf, and H. Hubner, "Analysis of Creep Pore Formation in Liquid-Phase Sintered Alumina," *Mater. Sci. Eng. A*, **234**, 932–5 (1997).

[138]H. M. Kerch, H. E. Burdette, and G. G. Long, "A High-Temperature Furnace for *In-Situ* Small-Angle Neutron-Scattering During Ceramic Processing," *J. Appl. Crystallogr.*, **28**, 604–10 (1995).

[139]D. Sen, T. Mahata, A. K. Patra, and S. Mazumder, "Effect of Sintering Temperature on Pore Growth in ZrO_2–8 mol% Y_2O_3 Ceramic Compact Prepared by Citric Acid Gel Route: A Small-Angle Neutron Scattering Investigation," *J. Alloys Compounds*, **364**, 304–10 (2004).

[140]D. Sen, A. K. Patra, S. Mazumder, and S. Ramanthan, "Pore Growth During Initial and Intermediate Stages of Sintering in ZrO_2–3 mol% Y_2O_3 Compact: A Small-Angle Neutron Scattering Investigation," *J. Alloys Compounds*, **361**, 270–5 (2003).

[141]T. Girardeau, S. Camelio, A. Traverse, F. Lignou, J. Allain, A. Naudon, and P. Guerin, "Relation Between the Optical Properties of Composite Si_3N_4 Thin Films with Embedded Cu Clusters and the Clusters Morphology: Irradiation Effects," *J. Appl. Phys.*, **90**, 1788–94 (2001).

[142]S. Rios and E. K. H. Salje, "Density Fluctuations in Alpha-Decay Self-Irradiated Zircon," *Appl. Phys. Lett.*, **84**, 2061–3 (2004).

[143]E. S. Kikkinides, K. L. Stefanopoulos, T. A. Steriotis, A. C. Mitropoulos, N. K. Kanellopoulos, and W. Treimer, "Combination of SANS and 3D Stochastic Reconstruction Techniques for the Study of Nanostructured Materials," *Appl. Phys. A*, **74**, S954–6 (2002).

[144]J. Mendez-Vivar, R. Mendoza-Serna, P. Bosch, V. H. Lara, and A. Ayala-Morales, "Simultaneous Polymerization of Mg and Zr Alkoxides," *Key Eng. Mater.*, **264–268**, 439–42 (2004).

[145]R. Guinebretiere, A. Dauger, A. Lecomte, and H. Vesteghem, "Tetragonal Zirconia Powders from the Zirconium n-Propoxide Acetylacetone Water Isopropanol System," *J. Non-Cryst. Solids*, **147**, 542–7 (1992).

[146]S. Botti, R. Coppola, F. Gourbilleau, and R. Rizk, "Photoluminescence from Silicon Nano-Particles Synthesized by Laser-Induced Decomposition of Silane," *J. Appl. Phys.*, **88**, 3396–401 (2000).

[147]R. F. Reidy, A. J. Allen, and S. Krueger, "Small Angle Neutron Scattering Characterization of Colloidal and Fractal Aerogels," *J. Non-Cryst. Solids*, **285**, 181–6 (2001).

[148]L. M. Liu, S. C. Li, B. Simmons, M. Singh, V. T. John, G. L. McPherson, V. Agarwal, P. Johnson, A. Bose, and N. Balsara, "Nanostructured Materials Synthesis in a Mixed Surfactant Mesophase," *J. Disper. Sci. Technol.*, **23**, 441–52 (2002).

[149]D. Sen, P. Deb, S. Mazumder, and A. Basumallick, "Microstructural Investigations of Ferrite Nanoparticles Prepared by Nonaqueous Precipitation Route," *Mater. Res. Bull.*, **35**, 1243–50 (2000).

[150]S. Lyonnard, J. R. Bartlett, E. Sizgek, K. S. Finnie, T. Zemb, and J. L. Woolfrey, "Role of Interparticle Potential in Controlling the Morphology of Spray-Dried Powders from Aqueous Nanoparticle Sols," *Langmuir*, **18**, 10386–97 (2002).

[151]A. J. Allen, G. G. Long, H. M. Kerch, S. Krueger, G. Skandan, H. Hahn, and J. C. Parker, "Sintering Studies of Nanophase Ceramic Oxides Using Small Angle Scattering," *Ceram. Int.*, **22**, 275–80 (1996).

[152]A. Wiedenmann, U. Lembke, A. Hoell, R. Muller, and W. Schuppel, "Magnetic Nanostructures in a Glass Ceramic Characterized by Small Angle Neutron Scattering," *Nanostruct. Mater.*, **12**, 601–4 (1999).

[153]U. Betz, S. S. Bhattacharya, and H. Hahn, "On the Development of a Low Temperature, Superplastic Nanocrystalline 5 mol.% Yttria Stabilised Zirconia: Synthesis, Processing and Mechanical Characterization," *Mater. Sci. Forum*, **343**, 539–44 (2000).

[154]A. Hoell, A. Wiedenmann, U. Lembke, and R. Kranold, "The Non-Magnetic Surface of Magnetic Particles in Nanostructured Glass Ceramics Studied by SANS," *Physica B*, **276**, 886–7 (2000).

[155]U. Betz, A. Sturm, J. F. Loeffler, W. Wagner, A. Wiedenmann, and H. Hahn, "Low-Temperature Isothermal Sintering and Microstructural Characterization of Nanocrystalline Zirconia Ceramics Using Small Angle Neutron Scattering," *Nanostruct. Mater.*, **12**, 689–92 (1999).

[156]T. Heinrich, F. Raether, O. Spormann, and J. Fricke, "SAXS Measurements of the Condensation in Mullite Precursors," *J. Appl. Crystallogr.*, **24**, 788–93 (1991).

[157]A. Dauger, A. Lecomte, H. Vesteghem, R. Guinebretiere, and D. Fargeot, "Small-Angle X-Ray-Scattering Study of Cordierite Sol–Gel Synthesis," *J. Appl. Crystallogr.*, **24**, 765–70 (1991).

[158]P. K. Sharma, H. Fischer, and A. F. Craievich, "Chemical and Structural Properties of Nickel Hydroxide Xerogels Obtained by the Sol–Gel Procedure in the Presence of Acetic Acid," *J. Am. Ceram. Soc.*, **82**, 1020–4 (1999).

[159]F. Cluzel, G. Larnac, and J. Phalippou, "Structure and Thermal Evolution of Mullite Aerogels," *J. Mater. Sci.*, **26**, 5979–84 (1991).

[160]K. Sinko, R. Mezei, L. Cser, G. Kali, and P. Fratzl, "SAS Experiments on Inorganic Gels," *Physica B*, **234**, 279–80 (1997).

[161]G. Beaucage, L. Guo, and J. Hyeon-Lee, "Kinetics of Morphological Development in Elastomer Modified Silica Xerogels," *Rubber Chem. Technol.*, **72**, 130–7 (1999).

[162]A. J. Hurd and P. Ho, "*In Situ* Light-Scattering Study of Particles Synthesized in a RF Silane Ammonia Glow-Discharge," *J. Aerosol Sci.*, **22**, 617–35 (1991).

[163]G. Beaucage, H. K. Kammler, R. Mueller, R. Strobel, N. Agashe, S. E. Pratsinis, and T. Narayanan, "Probing the Dynamics of Nanoparticle Growth in a Flame Using Synchrotron Radiation," *Nat. Mater.*, **3**, 370–4 (2004).

[164]R. W. Corkery and B. W. Ninham, "Low-Temperature Synthesis and Characterization of a Stable Colloidal TPA-Silicalite-1 Suspension," *Zeolites*, **18**, 379–86 (1997).

[165]J. D. F. Ramsay, "Characteristics of Inorganic Colloids," *Pure Appl. Chem.*, **64**, 1709–13 (1992).

[166]M. Singh, V. Agarwal, D. De Kee, G. McPherson, V. John, and A. Bose, "Shear-Induced Orientation of a Rigid Surfactant Mesophase," *Langmuir*, **20**, 5693–702 (2004).

[167]T. J. Su, J. R. Lu, Z. F. Cui, and R. K. Thomas, "Fouling of Ceramic Membranes by Albumins Under Dynamic Filtration Conditions," *J. Membr. Sci.*, **173**, 167–78 (2000).

[168]A. Gibaud, S. Hazra, C. Sella, P. Laffez, A. Desert, A. Naudon, and G. van Tendeloo, "Particle Layering in the Ceramic-Metal Thin Film Pt–Al_2O_3," *Phys. Rev. B*, **63**, 193407 (2001).

[169]S. Hazra, A. Gibaud, A. Desert, C. Sella, and A. Naudon, "Morphology of Nanocermet Thin Films: X-Ray Scattering Study," *Physica B*, **283**, 97–102 (2000).

[170]B. N. Nair, J. W. Elferink, K. Keizer, and H. Verweij, "Preparation and Structure of Microporous Silica Membranes," *J. Sol-Gel Sci. Technol.*, **8**, 471–5 (1997).

[171]E. S. Kikkinides, A. K. Stubos, K. P. Tzevelekos, A. C. Mitropoulos, and N. Kanellopoulo, "Ceramic Membranes—Characterization and Applications," *Stud. Surf. Sci. Catal.*, **120**, 687–713 (1999).

[172]C. Kluthe, T. Al-Kassab, J. Barker, W. Pyckhout-Hintzen, and R. Kirchheim, "Segregation of Hydrogen at Internal Ag/MgO (Metal/Oxide)-Interfaces as Observed by Small Angle Neutron Scattering," *Acta Mater.*, **52**, 2701–10 (2004).

[173]S. Hazra, A. Gibaud, and C. Sella, "Influence of Substrate Roughness on the Layering of Particles in Nanocermet Thin Films," *J. Phys. D*, **34**, 1575–8 (2001).

[174]H. Boukari, A. J. Allen, G. G. Long, J. Ilavsky, J. Wallace, C. C. Berndt, and H. Herman, "Small-Angle Neutron Scattering Study of the Role of Feedstock Particle Size on the Microstructural Behavior of Plasma-Sprayed YSZ Deposits," *J. Mater. Res.*, **18**, 624–34 (2003).

[175]J. Saroun, F. Eichhorn, A. Hempel, P. Lukas, B. Kolman, K. Neufuss, P. Mikula, and P. Strunz, "SANS Investigation of Plasma-Sprayed Materials Using a Double-Crystal Diffractometer," *Physica B*, **234**, 1011–3 (1997).

[176]P. Strunz, G. Schumacher, R. Vassen, and A. Wiedenman, "*In Situ* SANS Study of Pore Microstructure in YSZ Thermal Barrier Coatings," *Acta Mater.*, **52**, 3305–12 (2004).

[177]A. Kulkarni, J. Gutleber, S. Sampath, A. Goland, W. B. Lindquist, H. Herman, A. J. Allen, and B. Dowd, "Studies of the Microstructure and Properties of Dense Ceramic Coatings Produced by High-Velocity Oxygen-Fuel Combustion Spraying," *Mater. Sci. Eng. A*, **369**, 124–37 (2004).

[178]Z. Wang, A. Kulkarni, S. Deshpande, T. Nakamura, and H. Herman, "Effects of Pores and Interfaces on Effective Properties of Plasma Sprayed Zirconia Coatings," *Acta Mater.*, **51**, 5319–34 (2003).

[179]Y. I. Smirnov and N. O. Elyutin, "Investigation of Metallic and Ceramic Materials by Small-Angle Neutron Scattering," *Inorg. Mater.*, **40**, 548–53 (2004).

[180]T. Kamiyama, M. Sasaki, and K. Suzuki, "A Small-Angle Scattering Study of the Ceramization Process from Organic Polymer Precursors," *J. Appl. Crystallogr.*, **33**, 447–50 (2000).

[181]N. Maene, B. N. Nair, P. D'Hooghe, S. I. Nakao, and K. Keizer, "Silica-Polymers for Processing Gas Separation Membranes: High Temperature Growth of Fractal Structure," *J. Sol-Gel Sci. Technol.*, **12**, 117–34 (1998).

[182]M. Schallehn, M. Winterer, T. E. Weirich, U. Keiderling, and H. Hahn, "*In-Situ* Preparation of Polymer-Coated Alumina Nanopowders by Chemical Vapor Synthesis," *Chem. Vapor Depos.*, **9**, 40–4 (2003).

[183]M. Van Bruijnsvoort, R. Tijssen, and W. T. Kok, "Assessment of the Diffusional Behavior of Polystyrene Sulfonates in the Dilute Regime by Hollow-Fiber Flow Field Flow Fractionation," *J. Polym. Sci. B.*, **39**, 1756–65 (2001).

[184]C. B. W. Garcia, C. Lovell, C. Curry, M. Faught, Y. M. Zhang, and U. Wiesner, "Synthesis and Characterization of Block Copolymer/Ceramic Precursor Nanocomposites Based on a Polysilazane," *J. Polym. Sci. B, Polym. Phys.*, **41**, 3346–50 (2003).

[185]S. Renker, S. Mahajan, D. T. Babski, I. Schnell, A. Jain, J. Gutmann, Y. M. Zhang, S. M. Gruner, H. W. Spiess, and U. Wiesner, "Nanostructure and Shape Control in Polymer-Ceramic Hybrids from Poly(Ethylene Oxide)-Block-Poly (Hexyl Methacrylate) and Aluminosilicates Derived from them," *Macromol. Chem. Phys.*, **205**, 1021–30 (2004).

[186]E. Valiev, S. Bogdanov, A. Pirogov, A. Teplykh, A. Ostrouschko, and Y. Mogilnikov, "The Formation Processes of Oxide Phases from Polymer-Salt Complexes of Ammonium Molybdate and Tungstate," *Physica B*, **276**, 854–5 (2000).

[187]H. P. Martin, D. Kurtenbach, and E. Muller, "Nucleation and Crystallisation of Amorphous SiC from Polymeric Precursors," *Fresenius J. Anal. Chem.*, **361**, 576–7 (1998).

[188]J. J. Thomas, H. M. Jennings, and A. J. Allen, "The Surface Area of Hardened Cement Paste as Measured by Various Techniques," *Concrete Sci. Eng.*, **1**, 45–64 (1999).

[189]A. Heinemann, H. Hermann, and F. Haussler, "SANS Analysis of Fractal Microstructures in Hydrating Cement Paste," *Physica B*, **276**, 892–3 (2000).

[190]A. Heinemann, H. Hermann, K. Wetzig, F. Haussler, H. Baumbach, and M. Kroning, "Fractal Microstructures in Hydrating Cement Paste," *J. Mater. Sci. Lett.*, **18**, 1413–6 (1999).

[191]M. P. Fang, P. E. Sokol, J. Y. Jehng, and W. P. Halperin, "Neutron Diffraction Study of Cement," *J. Porous Mater.*, **6**, 55–9 (1999).

[192]F. Gaboriaud, A. Nonat, D. Chaumont, A. Craievich, and B. Hanquet, "Si-29 NMR and Small-Angle X-Ray Scattering Studies of the Effect of Alkaline Ions (Li+, Na+, and K+) in Silico-Alkaline Sols," *J. Phys. Chem. B*, **103**, 2091–9 (1999).

[193]I. G. Richardson, "The Nature of C–S–H in Hardened Cement Pastes," *Cem. Concrete Res.*, **29**, 1131–47 (1999).

[194]A. J. Allen and R. A. Livingston, "Relationship Between Differences in Silica Fume Additives and Fine-Scale Microstructural Evolution in Cement Based Materials," *Adv. Cem. Based Mater.*, **8**, 118–31 (1998).

[195]J. J. Thomas, H. M. Jennings, and A. J. Allen, "The Surface Area of Cement Paste as Measured by Neutron Scattering: Evidence for Two C–S–H Morphologies," *Cem. Concrete Res.*, **28**, 897–905 (1998).

[196]J. J. Thomas, H. M. Jennings, and A. J. Allen, "Determination of the Neutron Scattering Contrast of Hydrated Portland Cement Paste Using H_2O/D_2O Exchange," *Adv. Cem. Based Mater.*, **7**, 119–22 (1998).

[197]F. Haussler, M. Hempel, and H. Baumbach, "Long-Time Monitoring of the Microstructural Change in Hardening Cement Paste by SANS," *Adv. Cem. Res.*, **9**, 139–47 (1997).

[198]J. A. Janik, W. Kurdowski, R. Podsiadly, and J. Samseth, "Studies of Fractal Aspects of Cement," *Acta Phys. Pol. A*, **90**, 1179–84 (1996).

[199]F. Haussler, M. Hempel, F. Eichhorn, A. Hempel, and H. Baumbach, "Hydrating Cement Pastes as a Complex Disordered System," *Phys. Scripta*, **T57**, 184–9 (1995).

[200]D. Winslow, J. M. Bukowski, and J. F. Young, "The Fractal Arrangement of Hydrated Cement Paste," *Cem. Concrete Res.*, **25**, 147–56 (1995).

[201]F. Haussler, F. Eichhorn, and H. Baumbach, "Description of the Structural Evolution of Hydrating Portland-Cement Paste by SANS," *Phys. Scripta*, **50**, 210–4 (1994).

[202]D. N. Winslow, J. M. Bukowski, and J. F. Young, "The Early Evolution of the Surface of Hydrating Cement," *Cem. Concrete Res.*, **24**, 1025–32 (1994).

[203]R. E. Beddoe and K. Lang, "Effect of Moisture on Fractal Dimension and Specific Surface of Hardened Cement Paste by Small-Angle X-Ray-Scattering," *Cem. Concrete Res.*, **24**, 605–12 (1994).

[204]F. Haussler, F. Eichhorn, and H. Baumbach, "Small-Angle Neutron-Scattering on Hardened Cement Paste and Various Substances for Hydration," *Cem. Concrete Res.*, **24**, 514–26 (1994).

[205]F. Eichhorn, F. Haussler, and H. Baumbach, "Structural Studies on Hydrating Cement Pastes," *J. Phys. IV*, **3** [C8] 369–72 (1993).

[206]F. Adenot, L. Auvray, and J. C. Touray, "Determination of the Fractal Dimension of CSH Aggregates (Hydrated Calcium Silicates) of Different Origins and Compositions—Consequences for Studies of Cement Paste Durability," *C. R. Acad. Sci. II*, **317**, 185–9 (1993).

[207]A. J. Allen, "Time-Resolved Phenomena in Cements, Clays and Porous Rocks," *J. Appl. Crystallogr.*, **24**, 624–34 (1991).

[208]F. Haussler, F. Eichhorn, S. Rohling, and H. Baumbach, "Monitoring of the Hydration Process of Hardening Cement Pastes by Small-Angle Neutron-Scattering," *Cem. Concrete Res.*, **20**, 644–54 (1990).

[209]V. M. Castano, P. W. Schmidt, and H. G. Hornis, "Small-Angle Scattering Studies of the Pore Structure of Polymer-Modified Portland-Cement Pastes," *J. Mater. Res.*, **5**, 1281–4 (1990).

[210]R. H. Yang, B. Y. Liu, and Z. W. Wu, "Study on the Pore Structure of Hardened Cement Paste by SAXS," *Cem. Concrete Res.*, **20**, 385–93 (1990).

[211]J. J. Volkl, R. E. Beddoe, and M. J. Setzer, "The Specific Surface of Hardened Cement Paste by Small-Angle X-Ray-Scattering Effect of Moisture-Content and Chlorides," *Cem. Concrete Res.*, **17**, 81–8 (1987).

[212]A. J. Allen, R. C. Oberthur, D. Pearson, P. Schofield, and C. R. Wilding, "Development of the Fine Porosity and Gel Structure of Hydrating Cement Systems," *Philos. Mag. B*, **56** [3] 263–88 (1987).

[213]D. Pearson, A. J. Allen, C. G. Windsor, N. McN. Alford, and D. D. Double, "An Investigation on the Nature of Porosity in Hardened Cement Pastes using Small-Angle Neutron Scattering," *J. Mater. Sci.*, **18**, 430–8 (1983).

[214]D. Pearson and A. J. Allen, "A Study of Ultrafine Porosity in Hydrated Cements using Small-Angle Neutron Scattering," *J. Mater. Sci.*, **20**, 303–15 (1985).

[215]A. J. Allen, C. G. Windsor, V. S. Rainey, D. Pearson, D. D. Double, and N. McN. Alford, "A Small-Angle Scattering Study of Cement Porosities," *J. Phys. D*, **15**, 1817–33 (1982).

[216]L. C. Roess and C. G. Shull, "X-Ray Scattering at Small Angles by Finely-Divided Solids. II. Exact Theory for Random Distributions of Spheroidal Particles," *J. Appl. Phys.*, **18**, 308–13 (1947).

[217]J. S. Pedersen, "Form Factors of Block Copolymer Micelles with Spherical, Ellipsoidal and Cylindrical Cores," *J. Appl. Crystallogr.*, **33**, 637–40 (2000).

[218]G. Beaucage, H. K. Kammler, and S. E. Pratsinis, "Particle Size Distributions from Small-Angle Scattering Using Global Scattering Functions," *J. Appl. Crystallogr.*, **37**, 523–35 (2004).

[219]G. Beaucage, "Approximations Leading to a Unified Exponential/Power-Law Approach to Small-Angle Scattering," *J. Appl. Crystallogr.*, **28**, 717–28 (1995).

[220]J. A. Potton, G. J. Daniell, and B. D. Rainford, "Particle-Size Distributions from SANS Data Using the Maximum-Entropy Method," *J. Appl. Crystallogr.*, **21**, 663–8 (1988).

[221]G. Beaucage, H. K. Kammler, and S. E. Pratsinis, "Particle Size Distributions from Small-Angle Scattering Using Global Scattering Functions," *J. Appl. Crystallogr.*, **37**, 523–35 (2004).

[222]G. Beaucage, "Approximations Leading to a Unified Exponential/Power-Law Approach to Small-Angle Scattering," *J. Appl. Crystallogr.*, **28**, 717–28 (1995).

[223]P. R. Jemian, J. R. Weertman, G. G. Long, and R. D. Spal, "Characterization of 9Cr–1MoVNb Steel by Anomalous Small-Angle X-Ray-Scattering," *Acta Metall. Mater.*, **39**, 2477–87 (1991).

[224]P. W. Schmidt, "Small-Angle Scattering Studies of Disordered, Porous and Fractal Systems," *J. Appl. Crystallogr.*, **24**, 414–35 (1991).

[225]T. P. Rieker, S. Misono, and F. Ehrburger-Dolle, "Small-Angle X-Ray Scattering from Carbon Blacks: Crossover between the Fractal and Porod Regimes," *Langmuir*, **15**, 914–7 (1999).

[226]G. Beaucage, "Determination of Branch Fraction and Minimum Dimension of Mass-Fractal Aggregates," *Phys. Rev. E*, **70**, 031401 (2004).

[227]G. Beaucage, "Small-Angle Scattering from Polymeric Mass Fractals of Arbitrary Mass-Fractal Dimension," *J. Appl. Crystallogr.*, **29**, 134–46 (1996).

[228]T. P. Rieker, M. Hindermann-Bischoff, and F. Ehrburger-Dolle, "Small-Angle X-Ray Scattering Study of the Morphology of Carbon Black Mass Fractal Aggregates in Polymeric Composites," *Langmuir*, **16**, 5588–92 (2000).

[229]P. Thiyagarajan, J. E. Epperson, R. K. Crawford, J. M. Carpenter, T. E. Klippert, and D. G. Wozniak, "The Time-of-Flight Small-Angle Neutron Diffractometer (SAD) at IPNS, Argonne National Laboratory," *J. Appl. Crystallogr.*, **30**, 280–93 (1997).

[230]R. K. Crawford, "Neutron-Scattering Instrumentation for the National Spallation Neutron Source," *Physica B*, **241**, 107–9 (1997).

[231]D. Orthaber, A. Bergmann, and O. Glatter, "SAXS Experiments on Absolute Scale with Kratky Systems Using Water as a Secondary Standard," *J. Appl. Crystallogr.*, **33**, 218–25 (2000).

[232]U. Bonse and M. Hart, "Small-Angle X-Ray Scattering by Spherical Particles of Polystyrene and Polyvinyltoluene," *Appl. Phys. Lett*, **7**, 238–40 (1965).

[233]A. R. Drews, J. G. Barker, C. J. Glinka, and M. Agamalian, "Development of a Thermal-Neutron Double-Crystal Diffractometer for USANS at NIST," *Physica B*, **241**, 189–91 (1997).

[234]J. A. Lake, "An Iterative Method of Slit-Correcting Small Angle X-Ray Data," *Acta Crystallogr.*, **23**, 191–4 (1967).

[235]D. Schwahn, A. Miksovsky, H. Rauch, E. Seidl, and G. Zugarek, "Test of Channel-Cut Perfect Crystals for Neutron Small Angle Scattering Experiments," *Nucl. Instrum. Methods A*, **239**, 229–34 (1985).

[236]M. Agamalian, G. D. Wignall, and R. Triolo, "Optimization of a Bonse–Hart Ultra-Small-Angle Neutron Scattering facility by elimination of the rocking-curve wings," *J. Appl. Cryst.*, **30**, 345–52 (1997).

[237]C. T. Chantler, K. Olsen, R. A. Dragoset, A. R. Kishore, S. A. Kotochigova, and D. S. Zucker, *X-Ray Form Factor, Attenuation and Scattering Tables (version 2.1)*. National Institute of Standards and Technology, Gaithersburg, MD, 2005 (Available online at: http://physics.nist.gov/ffast [Access date]).

[238]A. J. Allen, T. A. Dobbins, J. Ilavsky, F. Zhao, A. Virkar, J. Almer, and F. DeCarlo, "Characterization of Solid Oxide Fuel Cell Layers by Computed X-Ray Microtomography and Small-Angle Scattering," *Ceram. Eng. Sci. Proc.*, **25** [3] 275–80 (2004).

[239]J. Schelten and W. Schmatz, "Multiple-Scattering Treatment for Small-Angle Scattering Problems," *J. Appl. Crystallogr.*, **13**, 385–90 (1980).

[240]C. A. Lucas, P. D. Hatton, S. Bates, T. W. Ryan, S. Miles, and B. K. Tanner, "Characterization of Nanometer-Scale Epitaxial Structures by Grazing-Incidence X-Ray-Diffraction and Specular Reflectivity," *J. Appl. Phys.*, **63**, 1936–41 (1988).

[241]C. H. Hsu, U. S. Jeng, H. Y. Lee, C. M. Huang, K. S. Liang, D. Windover, T. M. Lu, and C. Jin, "Structural Study of a Low Dielectric Thin Film Using X-Ray Reflectivity and Grazing Incidence Small Angle X-Ray Scattering," *Thin Solid Films*, **472**, 323–7 (2005).

[242]A. Kulkarni, A. Goland, H. Herman, A. J. Allen, T. A. Dobbins, F. DeCarlo, J. Ilavsky, G. G. Long, S. Fang, and P. Lawton, "Advanced Neutron and X-Ray Techniques for Insights into the Microstructure of EB-PVD Thermal Barrier Coatings," *Acta Mater.* (2005), submitted.

[243]L. E. Levine and G. G. Long, "X-Ray Imaging with Ultra-Small-Angle X-Ray Scattering as a Contrast Mechanism," *J. Appl. Crystallogr.*, **37**, 757–65 (2004).

[244]H. K. Kammler, G. Beaucage, R. Mueller, and S. E. Pratsinis, "Structure of Flame-Made Silica Nanoparticles by Ultra-Small-Angle X-Ray Scattering," *Langmuir*, **20**, 1915–21 (2004).

[245]D. Schaefer, J. M. Brown, D. P. Anderson, J. Zhao, K. Chokalingam, D. Tomlin, and J. Ilavsky, "Structure and Dispersion of Carbon Nanotubes," *J. Appl. Crystallogr.*, **36** [Part 3] 553–7 (2003).

[246]M. Hammel, P. Laggner, and R. Prassl, "Structural Characterisation of Nucleoside Loaded Low Density Lipoprotein as a Main Criterion for the Applicability as Drug Delivery System," *Chem. Phys. Lipids*, **123**, 193–207 (2003).

[247]C. E. Buckley, H. K. Birnbaum, J. S. Lin, S. Spooner, D. Bellmann, P. Staron, T. J. Udovic, and E. Hollar, "Characterization of H Defects in the Aluminium-Hydrogen System Using Small-Angle Scattering Techniques," *J. Appl. Cryst.*, **34**, 119–29 (2001). □

Andrew Allen is a physicist in the Ceramics Division of the Materials Science and Engineering Laboratory at the U.S. Department of Commerce's National Institute of Standards and Technology (NIST), Gaithersburg, Maryland. He received his Bachelor's degree in 1977 from the University of Oxford, England, and both his Master's degree (1978) and Doctorate (1981) from the University of Birmingham, England. From 1980 to 1991, he worked at the U.K. Atomic Energy Authority's (later AEA Technology) Harwell Laboratory in England, save for a 1 year sabbatical from 1988 to 1989 at Northwestern University, Evanston, Illinois. He has been based at NIST since 1991.

His main research interests lie in the development and application of advanced neutron and X-ray scattering methods for microstructure characterization. Recent applications have included ceramic thermal barrier coatings, nanocrystalline ceramics, modified cementitious materials, solid oxide fuel cell systems, and solution-mediated nanoparticulate assemblies.

Dr. Allen is the author or co-author of 50 archival journal publications, 50 conference proceedings and published reports, and has presented some 30 invited lectures. Currently, he serves on the research proposal review panels for small-angle scattering at both the NIST Center for Neutron Research and the Advanced Photon Source, Argonne National Laboratory. He is also a co-editor of the Journal of Applied Crystallography. Andrew Allen is a member of several professional societies, including the American Ceramic Society since 1992.